

Part I: Staggered index and 3D winding number of Kramers-degenerate bands

Alexander C. Tyner¹ and Pallab Goswami^{1,2}

¹ Graduate Program in Applied Physics, Northwestern University, Evanston, Illinois, 60208, USA and

² Department of Physics and Astronomy, Northwestern University, Evanston, Illinois, 60208, USA

(Dated: September 22, 2022)

For three-dimensional (3D) crystalline insulators, preserving space-inversion (\mathcal{P}) and time-reversal (\mathcal{T}) symmetries, the third homotopy class of two-fold, Kramers-degenerate bands is described by a 3D winding number $n_{3,j} \in \mathbb{Z}$, where j is the band index. It governs space group symmetry-protected, instanton or tunneling configurations of $SU(2)$ Berry connection, and the quantization of magneto-electric coefficient $\theta_j = n_{3,j}\pi$. We show that $|n_{3,j}|$ for realistic, *ab initio* band structures can be identified from a staggered symmetry-indicator $\kappa_{AF,j} \in \mathbb{Z}$ and the gauge-invariant spectrum of $SU(2)$ Wilson loops. The procedure is elucidated for 4-band and 8-band tight-binding models and *ab initio* band structure of Bi, which is a \mathbb{Z}_2 -trivial, higher-order, topological crystalline insulator. When the tunneling is protected by C_{nh} and D_{nh} point groups, the proposed method can also identify the signed winding number $n_{3,j}$. Our analysis distinguishes between magneto-electrically trivial ($\theta = 0$) and non-trivial ($\theta = 2s\pi$, with $s \neq 0$) topological crystalline insulators. In Part II, we demonstrate \mathbb{Z} -classification of θ by computing induced electric charge (Witten effect) on magnetic Dirac monopoles.

I. INTRODUCTION

Band structures of \mathcal{PT} symmetric materials are described by $2N \times 2N$ Bloch Hamiltonian matrix $\hat{H}(\mathbf{k}) = \sum_{j=1}^N E_j(\mathbf{k})\hat{P}_j(\mathbf{k})$, where N , $E_j(\mathbf{k})$, $\hat{P}_j(\mathbf{k})$ respectively correspond to the total number, the energy eigenvalues, and the projection operators of two-fold Kramers-degenerate bands, and \mathbf{k} is the wave vector. Since $E_j(\mathbf{k})$ and $\hat{P}_j(\mathbf{k})$ remain unchanged by $U(2)$ gauge transformations of Bloch wave functions of Kramers pairs, $\hat{H}(\mathbf{k})$ describes maps from *crystalline space groups* to the coset space $\frac{U(2N)}{U(2) \times \dots \times U(2)} = \frac{U(2N)}{[U(2)]^N}$. The objective of topological band theory is to classify such maps with appropriate bulk invariants.¹⁻¹⁴

For three-dimensional (3D) insulators, a 4-component unit vector $\hat{\mathbf{d}}_j(\mathbf{k})$ can be embedded in $\hat{P}_j(\mathbf{k})$, which wraps around the Brillouin zone (BZ) three-torus. Such instanton or tunneling configurations of $\hat{\mathbf{d}}_j(\mathbf{k})$ can be classified by the third spherical homotopy group $\pi_3(S^3) = \mathbb{Z}$, leading to the 3D winding number $n_{3j} \in \mathbb{Z}$. When $n_{3j} \neq 0$, $U(2)$ Berry connection $\mathbf{A}_j(\mathbf{k})$ inherits 3D tunneling configurations. Therefore, Wilson loop calculations can facilitate identification of $n_{3,j}$.

Exploiting rotation and mirror symmetries, $U(2)$ redundancy of Bloch wave functions can be reduced to $U(1) \times U(1)$ (or a smaller discrete sub-group). If such gauge-fixing procedure is properly implemented, the 3D winding number can be related to the Chern-Simons coefficient^{6,10,15-19}

$$\begin{aligned} \mathcal{CS}_j &= \frac{1}{8\pi^2} \int d^3k \epsilon^{abc} \text{Tr}[A_{a,j}\partial_b A_{c,j} + \frac{2i}{3}A_{a,j}A_{b,j} \\ &A_{c,j}] = \frac{n_{3,j}}{2}, \end{aligned} \quad (1)$$

and the magneto-electric coefficient or axion angle

$$\theta_j = 2\pi\mathcal{CS}_j = \pi n_{3,j}. \quad (2)$$

The primary goal of this work is to identify $|n_{3,j}|$ from symmetry analysis and the gauge-invariant spectrum of $SU(2)$ Wilson loops.

For concreteness, we will focus on materials, possessing \mathcal{P} and \mathcal{T} symmetries. For such systems, the numerical cost for Wilson loop calculations can be substantially reduced by symmetry analysis. The main idea is to first perform a *coarse classification* of bulk winding numbers, with fictitious ‘‘order parameter’’ type quantities, defined in momentum space on Miller hyper-cube, which are known as symmetry-indicators (SI).

The application of SIs for \mathcal{P} - and \mathcal{T} - symmetric topological insulators (TIs) was pioneered by Fu, Kane and Mele.^{3,4} They identified the strong, \mathbb{Z}_2 topological index (STI) $(-1)^{\nu_{0,j}} = (-1)^{n_{3,j}}$ from the product of parity eigenvalues at time-reversal-invariant-momentum (TRIM) points. The STI of a ground state, with m occupied bands is given by $\nu_{0,GS} = \sum_{j=1}^m \nu_{0,j} \pmod{2}$. When an odd (even) number of \mathbb{Z}_2 -non-trivial bands are occupied, $\nu_{0,GS}$ identifies the ground state as a non-trivial (trivial) insulator.

By construction, $\nu_{0,j}$ cannot distinguish (i) between $n_{3,j} = 0$, and $n_{3,j} = 2s \neq 0$, and (ii) between different odd integers. Since the ground states of topological crystalline insulators (TCIs) support a combination of \mathbb{Z}_2 -trivial bands and an even number of \mathbb{Z}_2 -non-trivial bands, their analysis requires new methods.^{13,14} This led to generalization of SIs,²⁰⁻³³ K -theory analysis,^{34,35} and the analysis of Wilson loop spectrum or Wannier charge centers (WCC).³⁶⁻⁴² However, we are not aware of any direct method for computing $n_{3,j}$ beyond the scope of \mathbb{Z}_2 -classification scheme^{6,10,15-19}. Therefore, it is difficult to predict whether TCIs can support quantized magneto-electric response with $\theta = 2s\pi$ and $s \neq 0$.

In this work, we will develop a comprehensive theoretical framework for computing $n_{3,j}$. We will introduce a staggered SI $\kappa_{AF,j} \in \mathbb{Z}$ for recognizing patterns of parity (and rotation) eigenvalues that lead to $n_{3,j} \neq 0$.

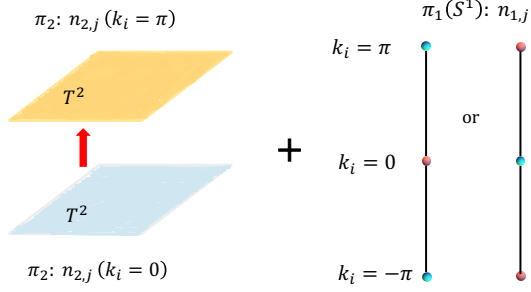


FIG. 1. Schematic of 3-dimensional tunneling configurations. The winding number $n_{3,j}$ corresponds to the change of 2-dimensional winding number $n_{2,j}$ of high-symmetry planes, which are equivalent to T^2 . 2-dimensional winding number identifies the presence of quantized, non-Abelian Berry flux for high-symmetry planes, and $|n_{3,j}| = |n_{2,j}(k_i = \pi) - n_{2,j}(k_i = 0)|$. The change of Berry flux must be accompanied by non-trivial 1-dimensional winding number ($n_{1,j}$) for one or more high-symmetry axes, along the tunneling direction. The converse is not true. While $n_{1,j}$ and $n_{2,j}$ can be obtained from Wilson loop calculations for Berry connection, this process can be guided by the staggered symmetry-indicator $\kappa_{AF,j}$.

Using $\kappa_{AF,j}$, the uniform \mathbb{Z}_4 index $\kappa_{1,j}$ ^{22,23}, and weak \mathbb{Z}_2 -indices ($\nu_{1,j}, \nu_{2,j}, \nu_{3,j}$)^{3,4}, following three classes of *non-trivial* band topology will be identified:

- (i) class A: 3D \mathbb{Z}_2 -topology, and $n_{3,j} = (2s_j + 1)$;
- (ii) class B: weak/2D \mathbb{Z}_2 -topology, and $n_{3,j} = 0$;
- (iii) class C: \mathbb{Z}_2 -trivial, 3D topology, and $n_{3,j} = 2s_j$.

For these three classes of bands, $\kappa_{AF,j}$ respectively displays odd integer, zero, and even integer values. After performing coarse-classification with SIs, we will show that $n_{3,j}$ can be calculated from tunneling configurations of $SU(2)$ Berry flux (see illustration of Fig. 1). This will be accomplished with a joint analysis of WCC for high-symmetry axes and in-plane Wilson loops for high-symmetry planes.

The manuscript is organized as follows. In Sec. II, we introduce $\kappa_{AF,j}$ and discuss its relationship with D -dimensional winding number. In Sec. III, we analyze O_h -symmetry-protected, tunneling configurations, using an analytically tractable 4-band model. Contrasting properties of Wilson loops and surface Dirac fermions for three classes A, B, and C are demonstrated. In Sec. IV, we describe essential features of D_{3d} -symmetry-protected instantons by considering a 4-band model of rhombohedral systems. In Sec. V, we compute $|n_{3,j}|$ for *ab initio* band structure of Bi. In Sec. VI, we conclude with a brief discussion of our results. In Appendix A, we present calculate of signed winding numbers of an 8-band tight-binding model of Bi.

II. STAGGERED INDEX AND HOMOTOPY CLASSIFICATION

We begin with a physical perspective on SIs of parity eigenvalues for D -dimensional, simple cubic systems. The TRIM points of D -dimensional BZ (vertices of Miller hyper-cube) can be written as

$$Q^i = \frac{1}{2} \sum_{a=1}^D l_a^i \mathbf{b}_a, \quad \text{with } i = 1, \dots, 2^D, \quad (3)$$

where \mathbf{b}_a are reciprocal vectors, and $l_a^i = 0, 1$. The parity eigenvalues of j -th band are Ising variables $\delta_j^i = \pm 1$, located on the vertices of Miller-cube. Topological information encoded in $2N \times 2N$ diagonal matrices

$$\mathcal{P}^i = \text{diag}[\delta_1^i \sigma_0, \dots, \delta_N^i \sigma_0], \quad (4)$$

can be extracted by using matrix-valued ‘‘order parameters’’ or SIs.

The \mathbb{Z}_2 STIs of constituent bands are given by

$$\prod_i \mathcal{P}^i = \text{diag}[(-1)^{\nu_{0,1}}, \dots, (-1)^{\nu_{0,N}}], \quad (5)$$

$$(-1)^{\nu_{0,j}} = \prod_{i=1}^{2^D} \delta_j^i. \quad (6)$$

The uniform or ferromagnetic indices^{22,23} are defined as

$$\kappa_{\mathbf{1}} = \frac{1}{2} \sum_{i=1}^{2^D} P^i = \text{diag}[\kappa_{1,1}, \dots, \kappa_{1,N}], \quad (7)$$

$$\kappa_{1,j} = \frac{1}{2} \sum_{i=1}^{2^D} \delta_j^i, \quad (8)$$

and $\kappa_{1,j}$ can acquire $(2^D + 1)$ values

$$\kappa_{1,j} = 0, \pm 1, \pm 2, \dots, \pm 2^{D-1}. \quad (9)$$

Due to the lack of band inversion, perfect ferromagnetic configurations [see Figs. 2(a) and 2(b)], describe topologically trivial bands, with $\kappa_{1,j} = \pm 2^{D-1}$. The uniform index of a ground state with m occupied bands is defined by

$$\kappa_{1,GS} = \sum_{j=1}^m \kappa_{1,j} \bmod 2^{D-1}, \quad \text{when } D > 1, \quad (10)$$

as it can be shifted by adding topologically trivial bands. Thus, $\kappa_{1,GS} = 0$, and $\kappa_{1,GS} = 2^{D-1} \times l$ with $l \in \mathbb{Z}$ correspond to topologically equivalent, trivial states, leading to the $\mathbb{Z}_{2(D-1)}$ -classification scheme for the ground state.

There exist

$$N_0 = \frac{2^D!}{[2^{(D-1)}!]^2} \quad (11)$$

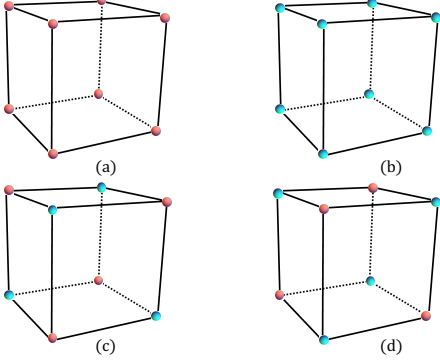


FIG. 2. (a)-(b) Ferromagnetic configurations of parity eigenvalues for topologically trivial bands. (c)-(d) Maximally staggered, Néel configurations of parity eigenvalues of topologically non-trivial bands. Eigenvalue $+1$ (-1) is denoted by light-red (cyan) dot.

Ising configurations, with 2^{D-1} positive, and 2^{D-1} negative parity eigenvalues, leading to $\kappa_{1,j} = 0$. We need new indicators to classify them. *Notably, both topologically non-trivial configurations at $D = 1$ possess $\kappa_{1,j} = 0$.* By focusing on maximally staggered, Néel configurations (see Fig. 2(c) and 2(d)), let us define

$$\begin{aligned} \kappa_{AF} &= \frac{1}{2} \sum_{i=1}^{2^D} (-1)^{l_1^i + l_2^i + \dots + l_D^i} \mathcal{P}^i \\ &= \text{diag}[\kappa_{AF,1}, \dots, \kappa_{AF,N}], \end{aligned} \quad (12)$$

$$\kappa_{AF,j} = \frac{1}{2} \sum_{i=1}^{2^D} (-1)^{l_1^i + l_2^i + \dots + l_D^i} \delta_j^i, \quad (13)$$

$$\kappa_{AF,GS} = \sum_{j=1}^m \kappa_{AF,j}. \quad (14)$$

Akin to $\kappa_{1,j}$, $\kappa_{AF,j}$ can also acquire $(2^D + 1)$ distinct values

$$\kappa_{AF,j} = 0, \pm 1, \pm 2, \dots, \pm 2^{D-1}, \quad (15)$$

As trivial bands with perfect ferromagnetic configurations lead to $\kappa_{AF,j} = 0$, $\kappa_{AF,GS} \neq 0$ cannot be deformed to 0 by adding topologically trivial bands. Therefore, the staggered index is a stable, \mathbb{Z} -valued SI, which can be used for all inversion-symmetric systems. By construction, $(-1)^{\kappa_{1,j}} = (-1)^{\kappa_{AF,j}} = (-1)^{\nu_{0,j}}$, and $(-1)^{\kappa_{1,GS}} = (-1)^{\kappa_{AF,GS}} = (-1)^{\nu_{0,GS}}$.

If our primary goal is to understand which configurations are capable of producing D -dimensional winding numbers, we can ignore N_0 configurations with $\kappa_{AF,j} = 0$. This can be seen from the explicit homotopy classifi-

cation of minimal model

$$\begin{aligned} \hat{H}(\mathbf{k}) &= \sum_{j=1}^{D+1} d_j(\mathbf{k}) \Gamma_j = t_p \sum_{j=1}^D \sin k_j \Gamma_j \\ &+ t_s [M - \Delta_1 \sum_{j=1}^D \cos k_j] \Gamma_{D+1}. \end{aligned} \quad (16)$$

of D -dimensional cubic topological insulators. Here t_p and t_s are hopping parameters, (M, Δ_1) are dimensionless tuning parameters, and Γ_j 's are $2^l \times 2^l$ mutually anti-commuting matrices, with $l \geq \lceil \frac{D+1}{2} \rceil$. The operation of \mathcal{P} is implemented as $\Gamma_{D+1} \hat{H}(-\mathbf{k}) \Gamma_{D+1} = H(\mathbf{k})$. Non-trivial D -dimensional band topology arises from instanton configurations of $O(D+1)$ unit vector $\hat{\mathbf{d}}(\mathbf{k}) = \mathbf{d}(\mathbf{k})/|\mathbf{d}(\mathbf{k})|$, which are classified by the D -th spherical homotopy group $\pi_D(S^D) = \mathbb{Z}$. The corresponding winding number

$$n_D = \frac{\Gamma(\frac{D+1}{2})}{2\pi^{\frac{D+1}{2}}} \int_{T^D} d^D k \epsilon_{i_1 \dots i_{D+1}} \hat{d}_{i_1} \partial_1 \hat{d}_{i_2} \dots \partial_D \hat{d}_{i_{D+1}}, \quad (17)$$

counts how many times the BZ D -torus T^D wraps around the unit-sphere S^D , and $\partial_a = \frac{\partial}{\partial k_a}$.

The TRIM points support parity eigenvalues $\delta_{\pm}^i = \pm \text{sgn}[d_{(D+1)}(\mathbf{Q}^i)]$ for $2^{(l-1)}$ -fold degenerate conduction (+) and valence (−) bands. When $t_s = 0$ and $t_p \neq 0$, they serve as hedgehogs of $O(D)$ unit vector, which can also be understood as merons of $O(D+1)$ unit vector, with hedgehog charge

$$n_h^i = (\text{sgn}(t_p))^D (-1)^{l_1^i + l_2^i + \dots + l_D^i}. \quad (18)$$

By combining the hedgehog charge and parity eigenvalues, we arrive at

$$n_D = \mp (\text{sgn}(t_p))^D \kappa_{AF,\pm}. \quad (19)$$

Therefore, the homotopy analysis of intra-band Berry connection provides information about

$$n_{D,\pm} = (\text{sgn}(t_p))^D \kappa_{AF,\pm} = \mp n_D. \quad (20)$$

Furthermore, we can rewrite n_D as

$$n_D = n_{D-1}(k_i = \pi) - n_{D-1}(k_i = 0), \quad (21)$$

which describes the change of $(D-1)$ -dimensional winding number along i -th high-symmetry direction, supporting band inversion. This scheme of dimensional reduction provides an intuitive way to think about instanton configurations of vector fields and non-Abelian Berry connection [see Fig. 1]. The staggered index precisely keeps track of such tunneling configurations.

The dimensional reduction for non-Abelian Berry connection can be performed by Wilson loop along j -th axis

$$W_{j,-}(\mathbf{k}_{\perp}) = \text{P exp} \left[i \int_{-\pi}^{\pi} A_{j,-}(k_j, \mathbf{k}_{\perp}) dk_j \right], \quad (22)$$

Parity eigenvalues ($\delta_\Gamma, \delta_R, \delta_X, \delta_M$)	Symmetry indicators ($\kappa_1; \kappa_{AF}; \nu_1, \nu_2, \nu_3$)	Class
1. (+1, +1, +1, +1)	(+4; 0; 0, 0, 0)	Trivial
2. (-1, -1, -1, -1)	(-4; 0; 0, 0, 0)	Trivial
3. (-1, +1, +1, +1)	(+3; -1; 0, 0, 0)	A
4. (+1, -1, -1, -1)	(-3; +1; 0, 0, 0)	A
5. (+1, -1, +1, +1)	(+3; +1; 1, 1, 1)	A
6. (-1, +1, -1, -1)	(-3; -1; 1, 1, 1)	A
7. (+1, +1, -1, +1)	(+1; +3; 1, 1, 1)	A
8. (-1, -1, +1, -1)	(-1; -3; 1, 1, 1)	A
9. (+1, +1, +1, -1)	(+1; -3; 0, 0, 0)	A
10. (-1, -1, -1, +1)	(-1; +3; 0, 0, 0)	A
11. (-1, -1, +1, +1)	(+2; 0; 1, 1, 1)	B
12. (+1, +1, -1, -1)	(-2; 0; 1, 1, 1)	B
13. (-1, +1, -1, +1)	(0; +2; 1, 1, 1)	C
14. (+1, -1, +1, -1)	(0; -2; 1, 1, 1)	C
15. (-1, +1, +1, -1)	(0; -4; 0, 0, 0)	C
16. (+1, -1, -1, +1)	(0; +4; 0, 0, 0)	C

TABLE I. Patterns of parity eigenvalues and symmetry indicators [see Eq. 28] for simple cubic systems, with $\Gamma = (0, 0, 0)$, $R = (1, 1, 1)$, $X = \{(1, 0, 0), (0, 1, 0), (0, 0, 1)\}$, and $M = (1, 1, 0), (0, 1, 1)$, and $(1, 0, 1)$. In Sec. III, we show that O_h -symmetry-protected tunneling configurations for simple cubic systems can be completely understood by considering the change of $SU(2)$ Berry flux along 4-fold or 3-fold axes. The staggered index tracks the bulk winding number, the number of normalizable surface Dirac cones, and the surface Hall conductivity of (001) and (111) surfaces.

where P indicates path-ordering, and WCC are given by

$$\bar{j}_-(\mathbf{k}_\perp) = \frac{1}{2\pi} \text{Im} [\ln(W_{j,-}(\mathbf{k}_\perp))]. \quad (23)$$

When two TRIM points with identical (opposite) parity eigenvalues are joined by Wilson loop, $W_{j,-} \rightarrow \mathbb{1}$ ($-\mathbb{1}$) which are the center elements of gauge group (spin groups which are double covers of special orthogonal groups). The element $-\mathbb{1}$ corresponds to π Berry phase or time-reversal polarization, and WCC describe interpolation between center elements as a function of $(D-1)$ -dimensional, transverse wave vector \mathbf{k}_\perp . In the following sections, we consider explicit examples of 3D simple cubic and rhombohedral models to elucidate the relationship between staggered index, bulk invariant and Wilson loops. To set the stage for such analysis, we provide simplified expressions of relevant SIs for some representative crystalline systems.

Parity eigenvalues ($\delta_\Gamma, \delta_X, \delta_L$)	Symmetry indicators ($\kappa_1; \kappa_{AF}; \nu_1, \nu_2, \nu_3$)	Class
1. (+1, +1, +1)	(+4; 0; 0, 0, 0)	Trivial
2. (-1, -1, -1)	(-4; 0; 0, 0, 0)	Trivial
3. (-1, +1, +1)	(+3; -1; 0, 0, 0)	A
4. (+1, -1, -1)	(-3; +1; 0, 0, 0)	A
5. (+1, -1, +1)	(+1; -3; 0, 0, 0)	A
6. (-1, +1, -1)	(-1; +3; 0, 0, 0)	A
7. (+1, +1, -1)	(0; +4; 0, 0, 0)	C
8. (-1, -1, +1)	(0; -4; 0, 0, 0)	C

TABLE II. Patterns of parity eigenvalues and symmetry indicators [see Eq. 29] for FCC crystals, with $\Gamma = (0, 0, 0)$, $X = \{(1, 1, 0), (0, 1, 1), (1, 0, 1)\}$, and $L = \{(1, 0, 0), (0, 1, 0), (0, 0, 1), (1, 1, 1)\}$. Notice that FCC crystals only support class A and class C bands, and class C bands exhibit maximally staggered, configurations of parity eigenvalues. Class C bands are important for describing topology of SnTe and PbTe. In contrast to simple cubic systems, tunneling of Berry flux for FCC systems occurs along (111) axis. Detailed analysis of tight-binding model and *ab initio* band structures of SnTe and PbTe will be presented in a separate work.

A. Staggered index of selected 3D systems

At $D = 3$, there are total $2^8 = 256$ configurations of parity eigenvalues. The perfect ferromagnetic (trivial bands) and Néel configurations (bands with maximal winding numbers) are respectively characterized by

$$(\kappa_{1,j}; \kappa_{AF,j}, \nu_{1,j}, \nu_{2,j}, \nu_{3,j}) = (\pm 4; 0; 0, 0, 0), \quad (24)$$

$$(\kappa_{1,j}; \kappa_{AF,j}, \nu_{1,j}, \nu_{2,j}, \nu_{3,j}) = (0; \pm 4; 0, 0, 0), \quad (25)$$

and the weak \mathbb{Z}_2 indices ($\nu_{1,j}, \nu_{2,j}, \nu_{3,j}$) identify odd vs. even integer distinction of 2D winding numbers for (100), (010), and (001) planes, passing through the high-symmetry point $(l_1, l_2, l_3) = (1, 1, 1)$. For example,

$$(-1)^{\nu_{1,j}} = \delta_j^{(1,1,1)} \delta_j^{(1,1,0)} \delta_j^{(1,0,0)} \delta_j^{(1,0,1)}, \quad (26)$$

$$\nu_{1,GS} = \sum_{j=1}^m \nu_{1,j} \text{ mod } 2. \quad (27)$$

Other $(2^8 - 4) = 252$ configurations of parity eigenvalues display imperfect ferromagnetic and staggered moments. Not all configurations are allowed by underlying crystal symmetries. For simple cubic systems (space groups 221 to 224) three X points (M) points support identical parity eigenvalue δ_X (δ_M). Therefore, only 16

Parity eigenvalues ($\delta_\Gamma, \delta_T, \delta_L, \delta_X$)	Symmetry indicators ($\kappa_1; \kappa_{AF}; \nu_1, \nu_2, \nu_3$)	Class
1. (+1, +1, +1, +1)	(+4; 0; 0, 0, 0)	Trivial
2. (-1, -1, -1, -1)	(-4; 0; 0, 0, 0)	Trivial
3. (-1, +1, +1, +1)	(+3; -1; 0, 0, 0)	A
4. (+1, -1, -1, -1)	(-3; +1; 0, 0, 0)	A
5. (+1, -1, +1, +1)	(+3; +1; 1, 1, 1)	A
6. (-1, +1, -1, -1)	(-3; -1; 1, 1, 1)	A
7. (+1, +1, -1, +1)	(+1; +3; 1, 1, 1)	A
8. (-1, -1, +1, -1)	(-1; -3; 1, 1, 1)	A
9. (+1, +1, +1, -1)	(+1; -3; 0, 0, 0)	A
10. (-1, -1, -1, +1)	(-1; +3; 0, 0, 0)	A
11. (-1, -1, +1, +1)	(+2; 0; 1, 1, 1)	B
12. (+1, +1, -1, -1)	(-2; 0; 1, 1, 1)	B
13. (-1, +1, -1, +1)	(0; +2; 1, 1, 1)	C
14. (+1, -1, +1, -1)	(0; -2; 1, 1, 1)	C
15. (-1, +1, +1, -1)	(0; -4; 0, 0, 0)	C
16. (+1, -1, -1, +1)	(0; +4; 0, 0, 0)	C

TABLE III. Patterns of parity eigenvalues and symmetry indicators [see Eq. 30] for rhombohedral systems, with $\Gamma = (0, 0, 0)$, $T = (1, 1, 1)$, $X = \{(1, 1, 0), (0, 1, 1), (1, 0, 1)\}$, and $L = (1, 0, 0), (0, 1, 0)$, and $(0, 0, 1)$. In Sec. IV, we show that D_{3d} -symmetry-protected tunneling configurations can be understood by considering the change of $SU(2)$ Berry flux along 3-fold axis. The staggered index tracks the bulk winding number, the number of normalizable surface Dirac cones, and the surface Hall conductivity of (111) surface. While addressing topology of *ab initio* band structure of Bi, we will encounter bands with 3-fold rotation eigenvalues $e^{\pm i\pi/3}$, and $e^{\pm i\pi}$. All SIs for $e^{\pm i\pi/3}$ will remain unchanged. For bands carrying $e^{\pm i\pi}$, κ_{AF} must be modified according to Eq. 31.

configurations can be realized, with SIs

$$\begin{aligned}
\kappa_{1,j} &= \frac{1}{2}(\delta_{\Gamma,j} + \delta_{R,j} + 3\delta_{X,j} + 3\delta_{M,j}), \\
\kappa_{AF,j} &= \frac{1}{2}(\delta_{\Gamma,j} - \delta_{R,j} - 3\delta_{X,j} + 3\delta_{M,j}), \\
\nu_{1,j} = \nu_{2,j} = \nu_{3,j} &= \frac{1}{2}(1 - \delta_R \delta_X). \quad (28)
\end{aligned}$$

Using $(\kappa_{1,j}; \kappa_{AF,j}; \nu_{1,j}, \nu_{2,j}, \nu_{3,j})$, we arrive at the coarse classification of Kramers-degenerate bands, listed in Table. I. The SIs for primitive tetragonal and orthorhombic systems are easily obtained by distinguishing different X and M points. Consequently, additional configurations can be allowed. But the main idea of tracking 3D winding numbers with $\kappa_{AF,j}$ remains unaffected.

For space groups 225-228, underlying FCC crystals lead to three X points and four L points. Therefore, only

8 configurations are allowed, which are listed in Table II, with SIs

$$\begin{aligned}
\kappa_{1,j} &= \frac{1}{2}(\delta_{\Gamma,j} + 3\delta_{X,j} + 4\delta_{L,j}), \\
\kappa_{AF,j} &= \frac{1}{2}(\delta_{\Gamma,j} + 3\delta_{X,j} - 4\delta_{L,j}), \\
\nu_{1,j} = \nu_{2,j} = \nu_{3,j} &= 0. \quad (29)
\end{aligned}$$

Importantly, FCC crystals do not support class B bands.

Rhombohedral systems are related to distorted FCC lattice. Due to rhombohedral distortion, (111) L point becomes inequivalent with other three L points, and is commonly known as the T point. Thus, rhombohedral systems allow 16 configurations of parity eigenvalues. The SIs are given by

$$\begin{aligned}
\kappa_{1,j} &= (\delta_{\Gamma,j} + \delta_{T,j} + 3\delta_{X,j} + 3\delta_{L,j}), \\
\kappa_{AF,j} &= (\delta_{\Gamma,j} - \delta_{T,j} + 3\delta_{X,j} - 3\delta_{L,j}), \\
\nu_{1,j} = \nu_{2,j} = \nu_{3,j} &= \frac{1}{2}(1 - \delta_T \delta_L). \quad (30)
\end{aligned}$$

and are listed in Table III. These SIs can be directly applied for analyzing *ab initio* band structures of materials like Bi, Sb, and Bi_2Se_3 , when bands possess 3-fold rotation eigenvalues $e^{\pm i\pi/3}$.

For bands with rotation eigenvalues $e^{\pm i\pi}$, Γ and T points support $n_h^\Gamma = \pm 3$, $n_h^T = \mp 3$, $n_h^X = \mp 1$, $n_h^L = \pm 1$ as hedgehog charge. Therefore, the staggered index of such bands is given by

$$\kappa_{AF,j}^{\pm\pi} = \frac{3}{2}(\delta_{\Gamma,j} - \delta_{T,j} + \delta_{L,j} - \delta_{X,j}) \quad (31)$$

Consequently, the staggered index of class A configurations 3-10 of Table III will be modified as

$$\kappa_{AF,j}^{\pm\pi} = -3, +3, +3, -3, -3, +3, +3, -3, \quad (32)$$

respectively. Class C configurations 13 – 16 support

$$\kappa_{AF}^{\pm\pi} = -6, +6, 0, 0 \quad (33)$$

Hence, maximally staggered configurations with rotation eigenvalues $e^{\pm i\pi}$ do not lead to 3D winding number. If the rotation data is not taken into account, Wilson loop calculations for 3-fold planes would guarantee that the correct magnitude of winding number is obtained.

For primitive hexagonal crystals, bands carrying rotation eigenvalues $e^{\pm i\frac{\pi}{6}}$ and $e^{\pm i\frac{\pi}{2}}$, the staggered index can be defined as

$$\begin{aligned}
\kappa_{AF,j}^{\pi/6} &= \frac{1}{2}(\delta_{\Gamma,j} - \delta_{A,j} - 3\delta_{X,j} + 3\delta_{L,j}), \\
\kappa_{AF,j}^{\pi/2} &= \frac{3}{2}(\delta_{\Gamma,j} - \delta_{A,j} - \delta_{X,j} + \delta_{L,j}). \quad (34)
\end{aligned}$$

For simple toy models of bands with $e^{\pm i\frac{\pi}{6}}$, K and H points can also participate in band inversion, and $\kappa_{AF,j}^{\pi/6}$ should be modified by adding $(\delta_K - \delta_H)$. Such examples can be found in Appendix A. Akin to rhombohedral systems, primitive hexagonal systems also support maximum staggered index ± 6 .

III. SIMPLE CUBIC SYSTEMS AND O_h INSTANTONS

To understand topology of O_h instanton configurations of Table I and $SU(2)$ Wilson loops, we consider a tight-binding model of two Kramers-degenerate bands, described by

$$H(\mathbf{k}) = \sum_{j=1}^5 d_j(\mathbf{k}) \Gamma_j. \quad (35)$$

Here Γ_j 's are 4×4 anti-commuting matrices, given explicitly as $\Gamma_{j=1,2,3} = \tau_1 \otimes \sigma_j$, $\Gamma_4 = \tau_2 \otimes \sigma_0$, and $\Gamma_5 = \tau_3 \otimes \sigma_0$, where $\sigma_{0,1,2,3}(\tau_{0,1,2,3})$ are 2×2 identity matrix and three Pauli matrices, operating on spin (orbital) index, respectively. Using T_{1u} and A_{1g} harmonics of O_h point group, we define the following map

$$\begin{aligned} d_j(\mathbf{k}) &= t_p \sin k_j, \text{ with } j = 1, 2, 3, \\ d_4(\mathbf{k}) &= M', \\ d_5(\mathbf{k}) &= t_s \left(M - \Delta_1 \sum_{j=1}^3 \cos k_j - \Delta_2 \sum_{i<j=1}^3 \cos k_i \cos k_j \right. \\ &\quad \left. - \Delta_3 \prod_{j=1}^3 \cos k_j \right), \end{aligned} \quad (36)$$

where $t_{p,s}$ are hopping parameters with units of energy, and $M, \Delta_1, \Delta_2, \Delta_3$ are dimensionless tuning parameters. For simplicity, the lattice constant has been set to unity. Parity and time-reversal symmetries are implemented as $\mathcal{P}^\dagger H(-\mathbf{k}) \mathcal{P} = H(\mathbf{k})$, $\mathcal{T}^\dagger H^*(-\mathbf{k}) \mathcal{T} = H(\mathbf{k})$, with $\mathcal{P} = \Gamma_5$, $\mathcal{T} = i\Gamma_{31} = i\tau_0 \otimes \sigma_2$, respectively, and $\Gamma_{ab} = [\Gamma_a, \Gamma_b]/(2i)$.

The pseudo-scalar mass $M' \neq 0$ breaks \mathcal{P} and \mathcal{T} symmetries, but preserves the combined \mathcal{PT} symmetry, $\Gamma_{24} H^*(\mathbf{k}) \Gamma_{24} = H(\mathbf{k})$, and Kramers-degeneracy. When $M' \neq 0$, the 4-band model describes generic magneto-electric insulators, and \mathcal{P} and \mathcal{T} symmetric topological insulators are obtained for $M' = 0$. While computing Chern-Simons coefficient, it is convenient to use $M' \rightarrow 0^+$, as a suitable regulator of Dirac string singularities at TRIM locations.

All salient properties of topological insulators follow from the $O(4)$ vector (d_1, d_2, d_3, d_5) , and the $SU(2)$ matrix

$$u(\mathbf{k}) = \hat{d}_5(\mathbf{k}) \sigma_0 + i \sum_{j=1}^3 \hat{d}_j(\mathbf{k}) \sigma_j. \quad (37)$$

At TRIM points parity eigenvalues of conduction (+) and valence (-) bands are given by $\pm \text{sgn}(d_5(\mathbf{Q}^i))$ and $u(\mathbf{k})$ maps to $SU(2)$ center elements $\pm \sigma_0$. The 3D wind-

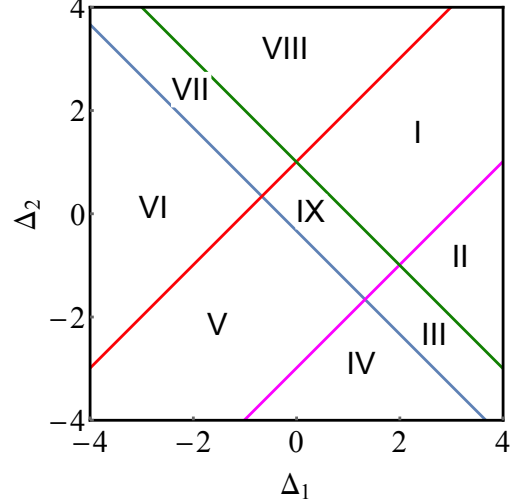


FIG. 3. Phase diagram of cubic model [Eq. 36], when $M = 1$ and $\Delta_3 = 2$. The configurations of parity eigenvalues, symmetry-indicators, and bulk winding numbers are summarized in Fig. 4. Along blue, green, red, and magenta colored lines, band gap can vanish at Γ , M , R , and X points, respectively. These lines are described by $d_5(\mathbf{Q}^i) = 0$.

ing number is determined by

$$\begin{aligned} n_3 &= \frac{1}{2\pi^2} \int_{T^3} d^3k \epsilon^{abcd} \hat{d}_a \partial_{k_x} \hat{d}_b \partial_{k_y} \hat{d}_c \partial_{k_z} \hat{d}_d, \\ &= \frac{1}{24\pi^2} \int_{T^3} d^3k \epsilon^{jlm} [(u^\dagger \partial_j u) u^\dagger \partial_l u] (u^\dagger \partial_m u), \end{aligned} \quad (38)$$

and the present model can realize

$$n_3 = \text{sgn}(t_p) \kappa_{AF,-} = \pm 1, \pm 2, \pm 3, \pm 4. \quad (39)$$

A representative phase diagram is shown in Fig. 3 for $M = +1$, $\Delta_3 = +2$. In Fig. 4, we display configurations of parity eigenvalues, SIs, and winding numbers for these phases.

As a consequence of cubic symmetry, all 4-fold symmetric planes exhibit D_{4h} symmetry. Consequently, they manifest as crystal-symmetry-enforced defects of Bloch map, and the $O(4)$ vector reduces to $O(3)$ vector. Topology of such planes can be classified by the second homotopy group $\pi_2(S^2) = \mathbb{Z}$, and 2D winding numbers

$$\begin{aligned} \mathbf{e}_{m,ab} \left(\frac{1}{2} \epsilon_{jab} k_j = 0, \pi \right) &= \\ \frac{1}{4\pi} \int_{T^2} dk_a dk_b \tilde{\mathbf{d}}(\mathbf{k}) \cdot \left(\partial_{k_a} \tilde{\mathbf{d}}(\mathbf{k}) \times \partial_{k_b} \tilde{\mathbf{d}}(\mathbf{k}) \right), \end{aligned} \quad (40)$$

correspond to mirror Chern numbers, describing quantized, non-Abelian Berry flux through high-symmetry

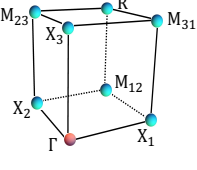
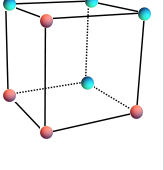
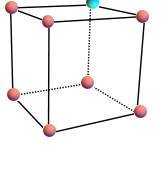
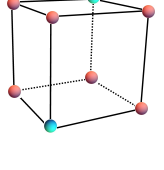
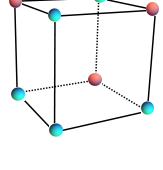
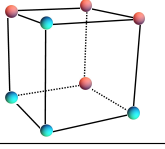
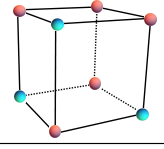
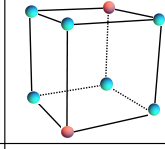
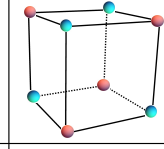
Indicators & bulk winding numbers	Phase I; Class A; Configuration 4	Phase II; Class C; Configuration 14	Phase III; Class A; Configuration 5	Phase IV; Class B; Configuration 11	Phase V; Class A; Configuration 10
Pattern of parity eigenvalues					
$(\kappa_1; \kappa_{AF}; \nu_1, \nu_2, \nu_3)$	$(-3; +1; 0, 0, 0)$	$(0; -2; 1, 1, 1)$	$(+3; +1; 1, 1, 1)$	$(+2; 0; 1, 1, 1)$	$(-1; +3; 0, 0, 0)$
$\mathfrak{C}_{m,ab}(\tilde{k} = \pi) - \mathfrak{C}_{m,ab}(\tilde{k} = 0) = n_3$	$(0) - (-1) = +1$	$(-1) - (+1) = -2$	$(+1) - (0) = +1$	$(+1) - (+1) = 0$	$(+2) - (-1) = +3$
Indicators & bulk winding numbers	Phase VI; Class C; Configuration 13	Phase VII; Class A; Configuration 7	Phase VIII; Class B; Configuration 12	Phase IX; Class C; Configuration 16	
Pattern of parity eigenvalues					
$(\kappa_1; \kappa_{AF}; \nu_1, \nu_2, \nu_3)$	$(0; +2; 1, 1, 1)$	$(+1; +3; 1, 1, 1)$	$(-2; 0; 1, 1, 1)$	$(0; +4; 0, 0, 0)$	
$\mathfrak{C}_{m,ab}(\tilde{k} = \pi) - \mathfrak{C}_{m,ab}(\tilde{k} = 0) = n_3$	$(+1) - (-1) = +2$	$(+1) - (-2) = +3$	$(-1) - (-1) = 0$	$(+2) - (-2) = +4$	

FIG. 4. Summary of symmetry-indicators and bulk winding numbers for nine homotopically distinct phases from Fig. 3. Under Phase I, time-reversal-invariant-momentum points $\Gamma = (0, 0, 0)$, $X_1 = (1, 0, 0)$, $X_2 = (0, 1, 0)$, $X_3 = (0, 0, 1)$, $M_{12} = (1, 1, 0)$, $M_{23} = (0, 1, 1)$, $M_{31} = (1, 0, 1)$, $R = (1, 1, 1)$ are labeled. Parity eigenvalue +1 (-1) of valence bands is indicated by red (cyan) dot. Three-dimensional winding number obeys Eq. 42, describing tunneling configurations of mirror Chern numbers along 4-fold axes. Therefore, for *ab initio* band structures of many simple cubic topological insulators, signed 3-dimensional winding numbers of constituent bands and ground state can be easily obtained from Wilson loop spectrum for D_{4h} symmetric mirror planes. This computational scheme is also applicable for other crystalline systems, when the tunneling is protected by C_{nh} and D_{nh} point group symmetries.

plane, and

$$\tilde{\mathbf{d}}(\mathbf{k}) = \{d_a(\mathbf{k}), d_b(\mathbf{k}), d_5(\mathbf{k})\} / \sqrt{d_a(\mathbf{k})^2 + d_b(\mathbf{k})^2 + d_5(\mathbf{k})^2}. \quad (41)$$

Phases with 3D winding numbers $n_{3,-} \neq 0$, support distinct values of quantized, non-Abelian Berry flux $2\pi\mathfrak{C}_{R,ab}$ for $k_j = 0, \pi$ planes. As a consequence of cubic symmetry, $n_{3,-}$ is precisely related to the tunneling configuration of non-Abelian Berry flux, along three principal 4-fold axes

$$n_{3,-} = \mathfrak{C}_{m,ab}(\frac{1}{2}\epsilon_{abj}k_j = \pi) - \mathfrak{C}_{m,ab}(\frac{1}{2}\epsilon_{abj}k_j = 0). \quad (42)$$

For the present model, we can express mirror Chern

numbers as

$$\begin{aligned} \mathfrak{C}_{m,ab}(\frac{1}{2}\epsilon_{abj}k_j = 0) &= \frac{1}{2}(2\delta_X - \delta_\Gamma - \delta_M), \\ \mathfrak{C}_{m,ab}(\frac{1}{2}\epsilon_{abj}k_j = \pi) &= \frac{1}{2}(2\delta_M - \delta_R - \delta_X), \end{aligned} \quad (43)$$

leading to the exact relationship $n_{3,-} = \kappa_{AF,-}$.

As weak topological insulators (Phase IV and Phase VIII) exhibit identical mirror Chern numbers for both $k_j = 0, \pi$ planes, they do not support 3D tunneling configurations. In contrast to this, Phase II and Phase VI, which are commonly denoted as weak topological insulators, carry 3D winding numbers $n_{3,-} = \pm 2$. Since weak \mathbb{Z}_2 indices do not carry information regarding sign of mirror Chern numbers, they cannot address the presence or absence of even integer winding numbers.

Finally, Phase IX is of particular interest, as it supports tunneling configurations of even integer valued mirror Chern numbers for all 4-fold mirror planes. Also note

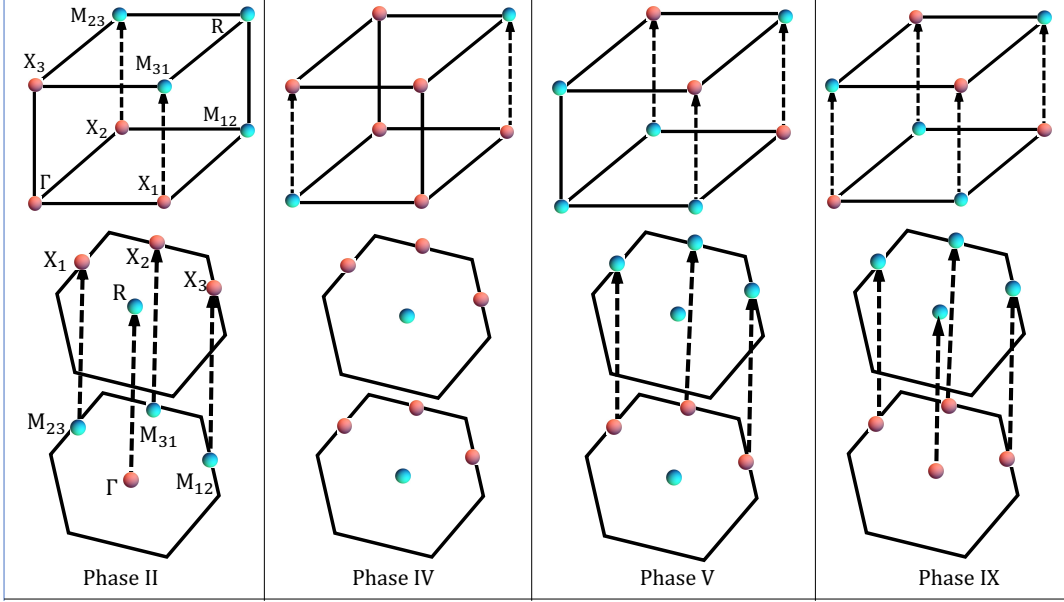


FIG. 5. Contrasting pictures of cubic-symmetry-protected instantons, when respectively viewed along 4-fold axis (001), and 3-fold axis (111). The dashed lines carry non-trivial one-dimensional winding numbers [see Eq. 44 and Eq. 45]. Wilson lines along these axes support π Berry phase, and the number of dashed lines counts the total number of 2-component, massless, Dirac fermions under open boundary conditions. For class B, weak topological insulator (Phase IV), the net one-dimensional winding number along z -axis vanishes, signifying the absence of tunneling. Consequently, anomalous Hall conductivity of [001] surface vanishes for Phase IV. The absence of tunneling is more directly seen from the perspective of 3-fold axis. Being a \mathbb{Z}_2 topological insulator, Phase V supports three non-trivial Wilson lines along [001] and [111] directions, and three gapless, Dirac fermions, and surface Hall conductivity $\pm \frac{3}{2}e^2/h$ for both surfaces. The number of surface Dirac fermions for Phase II for (001) ((111)) surface is 2 (4). But both surfaces possess Hall conductivity $\pm e^2/h$. Finally, phase IX displays 4 non-trivial Wilson lines along both directions, and supports four gapless Dirac fermions, and surface Hall conductivity $\pm 2e^2/h$.

that even integer mirror Chern numbers occur for $k_j = \pi$ planes of Phase V and $k_j = 0$ planes of Phase VII, leading to strong topological insulators with higher winding number $n_{3,-} = +3$.

Along any high-symmetry axis, joining \mathbf{Q}^i and \mathbf{Q}^j , the $O(4)$ vector (d_1, d_2, d_3, d_5) reduces to $O(2)$ vector, which can be classified by the fundamental group of circle $\pi_1(S^1) = \mathbb{Z}$. Let us consider four high-symmetry lines parallel to the \hat{z} axis, passing through $(k_x, k_y) = (0, 0), (\pi, 0), (0, \pi), (\pi, \pi)$. As these points correspond to TRIM locations of (001) surface BZ, we will denote them as $\bar{\mathbf{Q}} = \bar{\Gamma}, \bar{X}, \bar{Y}, \bar{M}$, respectively. The signed 1D winding numbers for high-symmetry axes are given by

$$\begin{aligned} n_1(\bar{\Gamma}) &= \frac{\text{sgn}(t_p)}{2}(\delta_X - \delta_\Gamma), \\ n_1(\bar{X}) &= n_1(\bar{Y}) = \frac{\text{sgn}(t_p)}{2}(\delta_M - \delta_X), \\ n_1(\bar{M}) &= \frac{\text{sgn}(t_p)}{2}(\delta_R - \delta_M), \end{aligned} \quad (44)$$

and these can be combined to write

$$\begin{aligned} n_{3,-} &= [-n_1(\bar{\Gamma}) - n_1(\bar{M}) + n_1(\bar{X}) + n_1(\bar{Y})] \\ &= \text{sgn}(t_p)\kappa_{AF,-}. \end{aligned} \quad (45)$$

When a high-symmetry axis supports non-trivial 1D winding number, it leads to normalizable 2-component, gapless Dirac fermions, under open boundary conditions along (001) direction. In the presence of infinitesimal regulator $M' \rightarrow 0^+$, the surface Hamiltonians in the vicinity of TRIM locations are given by

$$\begin{aligned} H(\bar{\mathbf{Q}} + \delta\mathbf{k}) &\approx \text{sgn}[n_{1D}(\bar{\mathbf{Q}})] [\cos(\bar{Q}_y)\delta k_y \sigma_1 \\ &\quad - \cos(\bar{Q}_x)\delta k_x \sigma_2] - \sigma_3 M'. \end{aligned} \quad (46)$$

Therefore, the chirality of Dirac cone and the surface Hall conductivity is determined by $\text{sgn}(n_{1D})$. While weak topological insulators (Phases IV and VIII) support Dirac cones at $(k_x, k_y) = (0, 0), (\pi, \pi)$, they come with opposite chirality, causing zero surface Hall conductivity. In contrast to this, Phases II and IX possess net surface Hall conductivity $\pm e^2/h, \pm 2e^2/h$, respectively. Thus, the staggered index provides a precise description of bulk topology and bulk-boundary correspondence.

The importance of staggered index can be further emphasized by considering tunneling configurations of Berry flux along the 3-fold axis (111) [see Fig. 5]. Phases II, IV, V, and IX respectively lead to 4, 0, 3, and 4 Dirac cones on (111) surface. But the signed 1D winding number and $\kappa_{AF,j}$ reveal that the Dirac cones for

Phase II at the center ($\bar{\Gamma}$) and the boundary of surface BZ (\bar{M}) possess opposite chirality. Thus, the net surface Hall conductivity of Phase II remains fixed to $\pm e^2/h$, despite the presence of 4 Dirac cones.

These collective properties of $O(4)$ vector control topology of $SU(2)$ Berry connection and the regularized Chern-Simons coefficient

$$\mathcal{CS}_-(M' \rightarrow 0^+) = \frac{n_{3,-}}{2}. \quad (47)$$

For numerical tight-binding models of *ab initio* band structure, the staggered index will provide a clear idea about the presence ($n_{3,j} \neq 0$) or absence ($n_{3,j} = 0$) of tunneling and the magnitude of winding number can be confirmed by Wilson loop calculations. Due to the D_{4h} symmetry of mirror planes, bands carrying 3D winding number exhibit fully connected, gapless spectrum for $W_j(\mathbf{k}_\perp)$, with $j = x, y, z$. Moreover, the mirror Chern numbers of different planes can be obtained from winding of WCC. Therefore, tunneling configurations along 4-fold axes of simple cubic systems can be fully characterized by gauge-invariant spectrum of $SU(2)$ Wilson loops.

Explicit calculations on analytically controlled 4-band model reveals the following features for Wilson loop W_{111} : (i) class A supports fully connected, gapless spectrum; (ii) class B shows gapped spectrum; and (iii) class C exhibits disconnected gapless spectrum. The number of gapless points are precisely counted by the number of non-trivial high-symmetry axes parallel to (111), or the staggered index [see Fig. 5]. The calculation of Berry flux for 3-fold planes has some subtleties, which are explained in the following sections.

IV. RHOMBOHEDRAL SYSTEMS AND D_{3d} INSTANTONS

In Ref. 43, an elegant four-band, tight-binding model was proposed by Mao *et. al* for describing Bi_2Se_3 . The 3D bulk Brillouin zone has the shape of a truncated octahedron, as shown in Fig. 6(a). The primitive reciprocal lattice vectors are given by

$$\begin{aligned} \mathbf{b}_1 &= (-1, -\sqrt{3}/3, b)g, \quad \mathbf{b}_2 = (1, -\sqrt{3}/3, b)g, \\ \mathbf{b}_3 &= (0, 2\sqrt{3}/3, b)g, \end{aligned} \quad (48)$$

where $b = 1/3$ and $g = 2\pi$, and the TRIM points are labeled by

$$\begin{aligned} \Gamma &= (0, 0, 0), \quad L = \{(1, 0, 0), (0, 1, 0), (0, 0, 1)\}, \\ T &= (1, 1, 1), \quad X = \{(1, 1, 0), (0, 1, 1), (1, 0, 1)\} \end{aligned} \quad (49)$$

and the SIs follow from Eq. 30. The underlying point group corresponds to D_{3d} and primary crystalline symmetries are: (i) 3-fold rotation about the [111] axis (C_{3z}); (ii) 2-fold rotations about $[1\bar{1}0]$, $[10\bar{1}]$, and $[01\bar{1}]$ axes

(C_2); (iii) mirror symmetries for 2-fold planes $\mathcal{M}_{1\bar{1}0}$, $\mathcal{M}_{10\bar{1}}$, and $\mathcal{M}_{01\bar{1}}$; (iv) space-inversion symmetry (\mathcal{P}).

The Bloch Hamiltonian has the form of Eq. 35 and $\mathbf{d}(\mathbf{k})$ is given by

$$\begin{aligned} d_1(\mathbf{k}) &= -2A_{14} \sin w(\sin k_{a2} - \sin k_{a3}) \\ &\quad + 2B_{14}[\sin k_{g1} + \cos w(\sin k_{g2} + \sin k_{g3})], \\ d_2(\mathbf{k}) &= -2B_{14} \sin w(\sin k_{g2} - \sin k_{g3}) \\ &\quad - 2A_{14}[\sin k_{a1} + \cos w(\sin k_{a2} + \sin k_{a3})], \\ d_3(\mathbf{k}) &= 2A_{12} \sum_{i=1}^3 \sin k_{ai}, \\ d_4(\mathbf{k}) &= -2B_{12} \sum_{i=1}^3 \sin k_{gi}, \\ d_5(\mathbf{k}) &= 2A_{11} \sum_{i=1}^3 \cos k_{ai} + 2B_{11} \sum_{i=1}^3 \cos k_{gi} + m_{11}, \end{aligned} \quad (50)$$

where $w = -2\pi/3$, $k_{ai} = \mathbf{k} \cdot \mathbf{a}_i$ and $k_{gi} = \mathbf{k} \cdot \mathbf{g}_i$, $a_1 = (a, 0, 0)$, $a_2 = (-\frac{a}{2}, \frac{\sqrt{3}a}{2}, 0)$, $a_3 = (-\frac{a}{2}, -\frac{\sqrt{3}a}{2}, 0)$, $g_1 = (0, \frac{a}{\sqrt{3}}, c)$, $g_2 = (-\frac{a}{2}, -\frac{\sqrt{3}a}{6}, c)$, and $g_3 = (\frac{a}{2}, -\frac{\sqrt{3}a}{6}, c)$, and $c/a = b = 1/3$.

Under symmetry operations of D_{3d} point group, ($d_1(\mathbf{k}), d_2(\mathbf{k}), d_3(\mathbf{k}), d_4(\mathbf{k}),$ and $d_5(\mathbf{k})$) respectively transform as E_u -doublet, A_{2u} -singlet, A_{1u} -singlet, and A_{1g} -singlet. The operations of \mathcal{P} , \mathcal{T} , C_{3z} , C_{2x} , and \mathcal{M}_{YZ} symmetries are respectively implemented with

$$\Gamma_5, i\Gamma_{31}, e^{i\pi/3}\Gamma_{12}, i\Gamma_{14}, \text{ and } \Gamma_5\Gamma_{14} = \Gamma_{23}.$$

The presence of A_{2u} harmonic is a natural consequence of crystalline symmetry. It does not affect symmetry-indicators and bulk winding numbers, and universal topological properties are captured by 4-component vector (d_1, d_2, d_4, d_5), and the $SU(2)$ matrix $u(\mathbf{k}) = \hat{d}_5(\mathbf{k})\sigma_0 + i\hat{d}_1(\mathbf{k})\sigma_1 + i\hat{d}_2(\mathbf{k})\sigma_2 + i\hat{d}_4(\mathbf{k})\sigma_3$. Thus, Eq. 50 is a non-trivial example of 4-band model, where a homotopically non-trivial $O(4)$ vector remains embedded within $O(5)$ unit vector.

The current model is sufficient for capturing 14 out of 16 configurations (except $\kappa_{AF} = \pm 4$) of Table III and 3D winding numbers

$$n_{3,-} = -\text{sgn}(B_{12})\kappa_{AF,-} = \pm 1, \pm 2, \pm 3, \quad (51)$$

for $u(\mathbf{k})$. After regulating

$$d_3(\mathbf{k}) \rightarrow d'_3(\mathbf{k}) = M' + d_3(\mathbf{k}),$$

the regularized Chern-Simons coefficient of valence bands is given by $\mathcal{CS}_-(M' \rightarrow 0^+) = \frac{n_{3,-}}{2}$. A representative phase diagram involving nine phases are shown in Fig. 6(c). A summary of SIs, bulk winding numbers, and Wilson loop analysis are presented in Fig. 7.

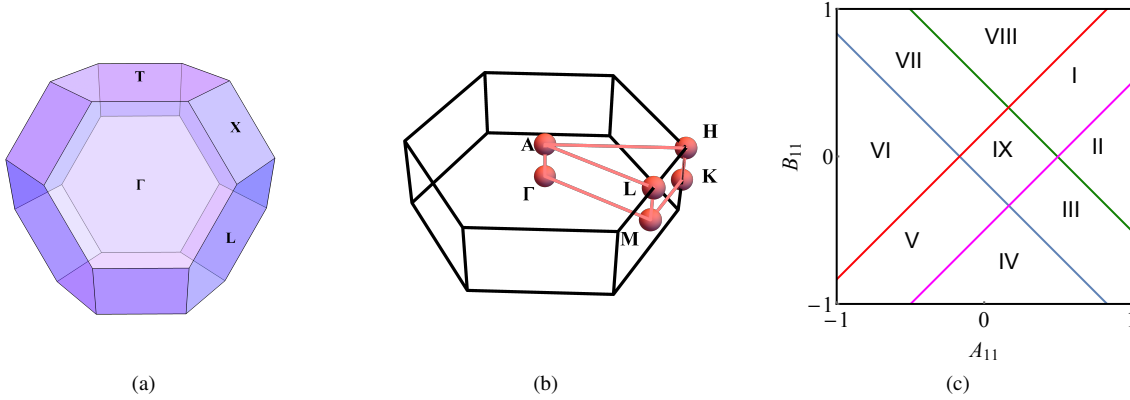


FIG. 6. (a) For the primitive unit cell, the bulk Brillouin zone of rhombohedral systems has the shape of a truncated octahedron, with high-symmetry points Γ , T , X , and L . (b) For addressing topology of 3-fold planes, it is convenient to work with conventional unit cell, which leads to a hexagonal Brillouin zone. The volume of hexagonal Brillouin zone is three times larger than the volume of truncated octahedron. The Γ , T , X , and L points of truncated octahedron respectively map to the Γ , A , M , and L points of hexagonal Brillouin zone. (c) The phase diagram of rhombohedral model [Eq. 50] when $m_{11} = +1$. Along blue, green, red, and magenta colored lines, band gap can vanish at Γ , X , T , and L points, respectively. These lines are described by $d_5(\mathbf{Q}^i) = 0$.

A. $SU(2)$ Wilson loops

Along all high-symmetry axes joining two TRIM points, the $O(5)$ vector reduces to different $O(2)$ vectors. For understanding the presence or absence of tunneling, we first consider 1D winding numbers for high-symmetry axes, which are parallel to \hat{z} . Using hexagonal BZ, these lines can be identified as $\Gamma T \equiv \Gamma A$ passing through $(k_x, k_y) = (0, 0)$, and three $XL \equiv ML$ lines, respectively passing through $(2\pi, 0)$, $(\pi, \sqrt{3}\pi)$, and $(-\pi, \sqrt{3}\pi)$. The signed 1D winding numbers and 3D winding number can be related as

$$\begin{aligned} n_1(\Gamma T) &= \text{sgn}(B_{12}) \frac{1}{2} (\delta_{T,-} - \delta_{\Gamma,-}), \\ n_1(XL) &= \text{sgn}(B_{12}) \frac{1}{2} (\delta_{L,-} - \delta_{X,-}), \\ n_1(\Gamma T) + 3n_1(XL) &= n_{3,-} = -\text{sgn}(B_{12}) \kappa_{AF,-}. \end{aligned} \quad (52)$$

When n_1 is non-trivial, $SU(2)$ Wilson loop $W_{z,-}(k_x, k_y)$ displays gapless spectrum. The WCC spectrum $\tilde{z}(k_x, k_y)$ for classes A (Phase V), B (Phase II), and C (Phase IV) are shown in Figs. 8(a)-8(c). As 3-fold planes lack mirror symmetry, class C bands exhibit disconnected, gapless spectrum (as emphasized for simple cubic systems). Therefore, the full connectivity of WCC is not an essential criterion to determine 3D winding number.

For 3-fold XY planes, $O(5)$ vector does not reduce to $O(3)$ vector. Thus, 2D winding numbers must be found

from in-plane Wilson loops, defined as

$$W_j(C) = \text{P exp} \left[i \oint \sum_{a=1}^2 A_{a,j}(\mathbf{k}(l)) \frac{dk_a}{dl} dl \right]. \quad (53)$$

It describes $SU(2)$ Berry phase accrued by the j -th Kramers-degenerate band, when parallel-transported along a closed, non-intersecting curve C , parameterized by $\mathbf{k}(l)$. As an element of $SU(2)$ group, W_j can be written as,

$$W_j(C) = \exp \left[i \theta_j \hat{\Omega}_j \cdot \boldsymbol{\sigma} \right]. \quad (54)$$

By employing non-Abelian Stokes theorem, the gauge invariant angle θ_j can be related to the magnitude of $SU(2)$ Berry flux enclosed by the loop C .^{44,45} The in-plane loop will be calculated with 3-fold symmetry preserving contours [see Fig. 8(d)], and the area of the loop will be gradually increased from 0 to the area of hexagonal BZ. The magnitude of relative Chern number $|\mathfrak{C}_{3,XY;j}|$ is found from

$$|\mathfrak{C}_{3,XY;j}| = \frac{1}{2\pi} |\theta_j(k_0 = k_b) - \theta_j(k_0 = 0)|. \quad (55)$$

The computation of 2D winding numbers can be further simplified by taking advantage of crystalline symmetry, as explained in Figs. 8(e) and 8(f). The results for in-plane Wilson loops for Phases I, IV, and V are shown in Figs. 8(h)-8(i).

To further elaborate on important differences with simple cubic systems, we study YZ mirror planes, passing through $k_x = 0, 2\pi$. For these planes $d_2 = d_3 = 0$, and we can compute mirror Chern numbers from the

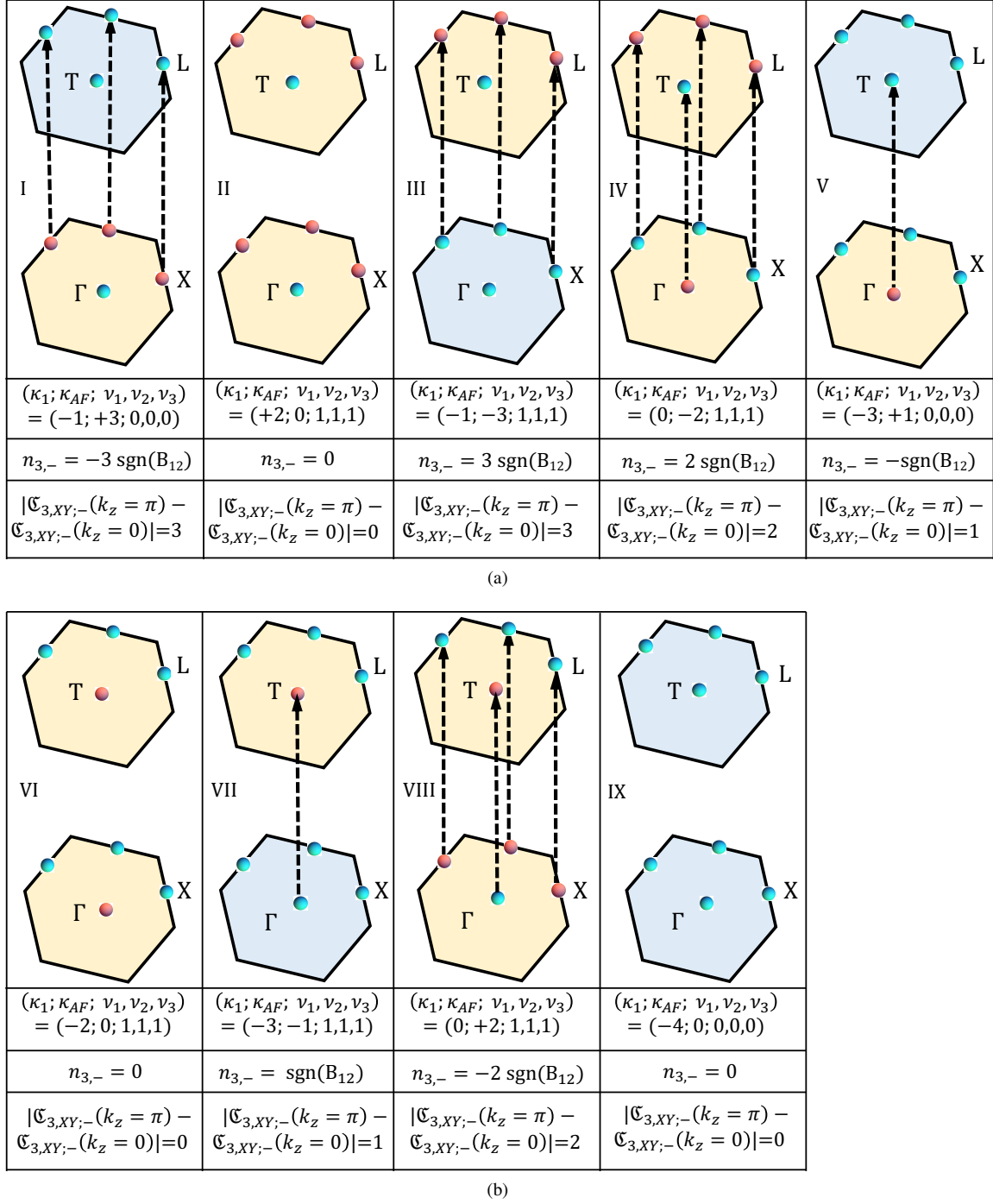


FIG. 7. Tunneling configurations, symmetry-indicators, and bulk winding numbers for nine homotopically distinct, rhombohedral phases of Fig. 6(c). Parity eigenvalue +1 (-1) of valence bands is indicated by red (cyan) dot. All three types of band topology can be succinctly understood in terms of tunneling configurations of C_3 -symmetry protected Berry flux through XY planes. The \mathbb{Z}_2 trivial (non-trivial) planes are colored blue (yellow).

$O(3)$ vector (d_1, d_4, d_5) . While class A bands support mirror Chern numbers

$$\mathfrak{C}_{m,YZ}(k_x = 0) = \mathfrak{C}_{m,YZ}(k_x = 2\pi) = \pm 1, \quad (56)$$

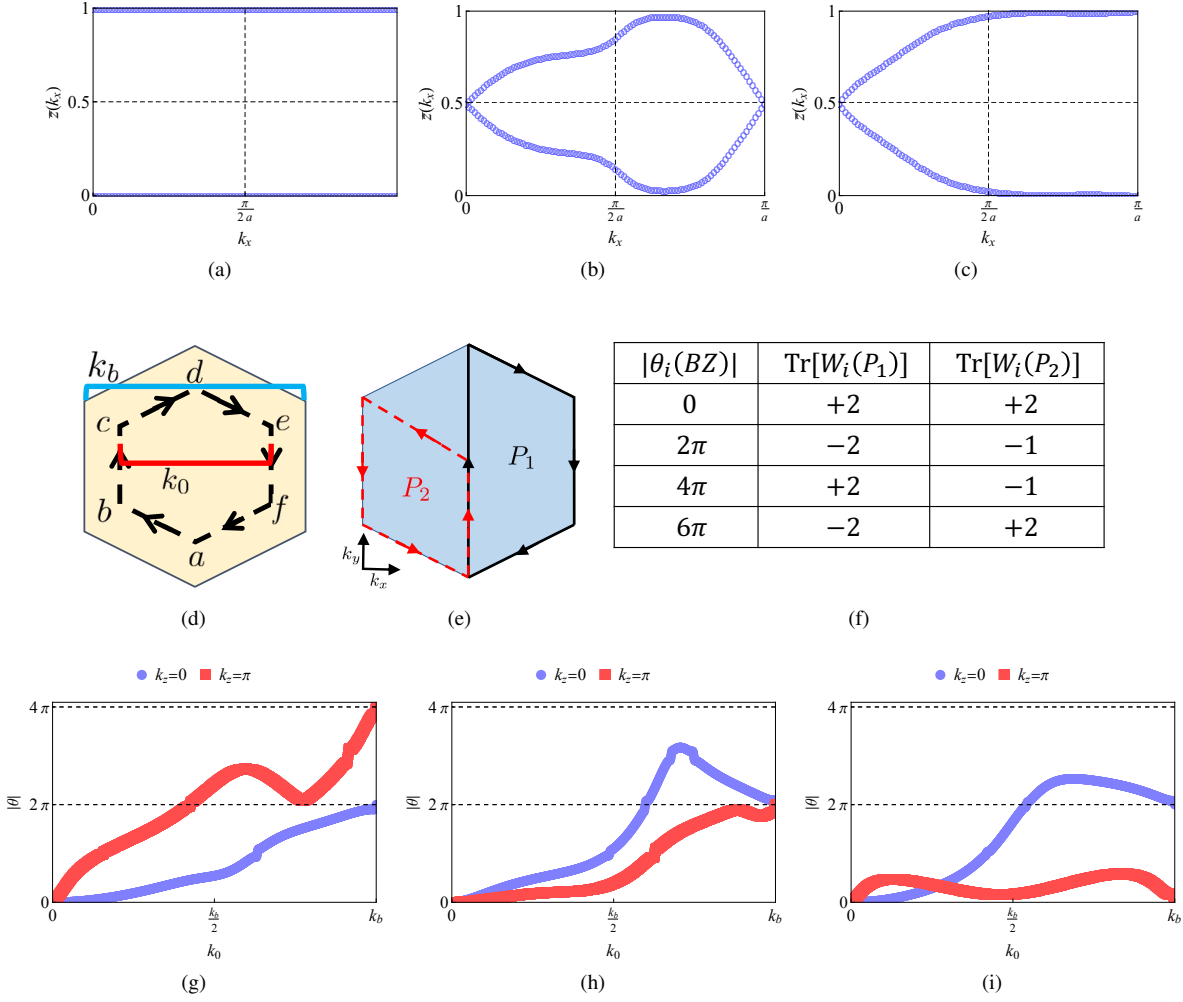
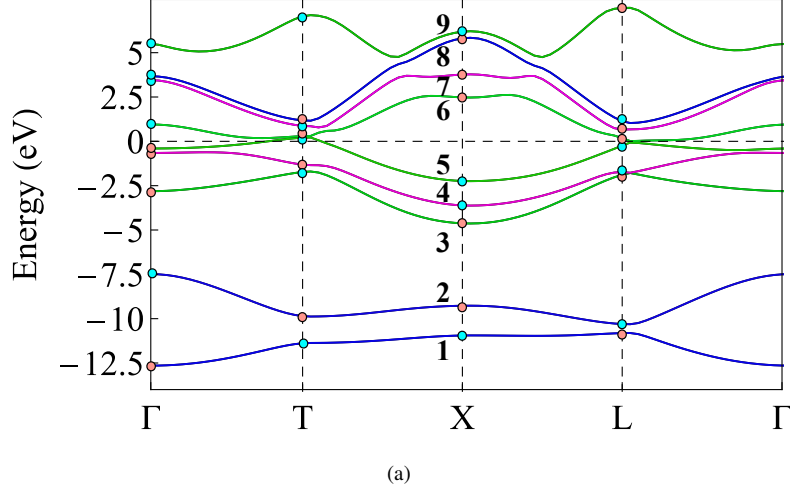


FIG. 8. Summary of Wilson loop analysis. (a) Phase II (class B bands with $n_{3,j} = 0$) exhibits gapped spectrum. (b) Phase IV (class C bands with $n_{3,j} = \pm 2$) supports disconnected, gapless spectrum. (c) Phase V (class A bands with $n_{3,j} = \pm 1$) exhibits fully connected, gapless spectrum. (d) Schematic of 3-fold symmetric contour, around which Wilson loop is calculated for $k_z = 0, \pi$ planes. The yellow region represents the first Brillouin zone of xy planes. The size of contour is parameterized by k_0 . When $k_0 = k_b$, the path encloses the full Brillouin zone. (e) To reduce computational cost, we can further exploit symmetry of 3-fold planes and compute in-plane Wilson loops along high-symmetry paths P_1 and P_2 . (f) If a Kramers pair supports quantized flux $|\theta_i| = 2l_i\pi$ through the hexagonal Brillouin zone, P_1 and P_2 respectively enclose $l_i\pi$, and $\frac{2}{3}l_i\pi$. Hence, from the trace of Wilson loops, we can distinguish between bands, possessing two-dimensional winding numbers $|\mathcal{C}_{3,XY;i}| = 0, 1, 2, 3$ for different hexagonal planes. (g) For Phase I $k_z = 0$ and π planes respectively possess $|\mathcal{C}_{3,XY;i}| = 1, |\mathcal{C}_{3,XY;i}| = 2$. (h) For Phase IV both planes possess $|\mathcal{C}_{3,XY;i}| = 1$. (i) For phase V, $k_z = 0, \pi$ planes carry $|\mathcal{C}_{3,XY;i}| = 1, 0$, respectively. By applying an infinitesimal \mathcal{T} -breaking, training field we obtain signed $\mathcal{C}_{3,XY;i}$.

no tunneling occurs along 2-fold axis. In contrast to this, Class B and Class C bands do not possess any mirror Chern numbers. Thus, $n_{3,-}$ cannot be identified from $\mathcal{C}_{m,YZ}$. With analytical and numerical insights gained for $R\bar{3}m$ instantons, in the following section we address topology of *ab initio* band structure of Bi.

V. AB INITIO BAND STRUCTURE OF BISMUTH

Though originally considered to be a topologically trivial system, refined symmetry-indicators show that the ground state admits both higher-order and rotational-symmetry-protected crystalline topology.^{46–52} Does this imply the existence of even integer 3D winding number? We will affirmatively answer this question with a combined analysis of κ_{AF} and \mathcal{C}_3 -symmetry-protected tunneling configurations of non-Abelian Berry flux. This



Band index i	C_{3z} eigenvalues	Parity eigenvalues ($\delta_\Gamma, \delta_T, \delta_X, \delta_L$)	\mathbb{Z}_4 and weak \mathbb{Z}_2 indices ($\kappa_{1,i}; \nu_{1,i}, \nu_{2,i}, \nu_{3,i}$)	Staggered index $\kappa_{AF,i}$	Class
1	$e^{\pm i\frac{\pi}{3}}$	(+1, -1, -1, +1)	(0; 1, 1, 1)	-2	C
2	$e^{\pm i\frac{\pi}{3}}$	(-1, +1, +1, -1)	(0; 1, 1, 1)	+2	C
3	$e^{\pm i\frac{\pi}{3}}$	(+1, -1, +1, +1)	(+3; 1, 1, 1)	+1	A
4	$e^{\pm i\frac{\pi}{3}}$	(+1, +1, -1, -1)	(-2; 1, 1, 1)	0	B
5	$e^{\pm i\pi}$	(+1, -1, -1, -1)	(-3; 0, 0, 0)	+3	A
6	$e^{\pm i\frac{\pi}{3}}$	(-1, +1, +1, +1)	(+3; 0, 0, 0)	-1	A
7	$e^{\pm i\frac{\pi}{3}}$	(-1, -1, +1, +1)	(+2; 1, 1, 1)	0	B
8	$e^{\pm i\pi}$	(-1, +1, +1, -1)	(0; 1, 1, 1)	-6	C
9	$e^{\pm i\frac{\pi}{3}}$	(-1, -1, -1, +1)	(-1; 1, 1, 1)	-3	A

(b)

FIG. 9. (a) Bulk band structure of Bi along high symmetry paths of primitive Brillouin zone (Fig. 6(a)) and light-red (cyan) dots denote parity eigenvalues +1 (-1) at time-reversal-invariant momentum points. Class A, Class B and Class C bands are respectively colored as green, purple, and blue. (b) Summary of symmetry data and indicators for various Kramers-degenerate bands of bismuth. According to Table III bands $i = 1$ through 9 have parity eigenvalue configuration numbers 14, 13, 5, 12, 4, 3, 11, 13, and 8, respectively. We have used Eq. 30, and 31 to account for the rotation eigenvalues. The hypothetical insulator with fully occupied bands 1 through 5 is a higher-order topological insulator, with ground state indicators given by Eq. 57. To understand these indicators one must consider the combined effects of bands 3, 4, and 5. If the chemical potential is placed between bands 1 and 2, the resulting insulator will exhibit class C topology. In contrast to this, all ground state indicators would vanish for the insulator obtained by placing the chemical potential between bands 2 and 3.

tunneling configuration also underpins the diversity of topological phases that can be realized by varying the number of buckled honeycomb layers and the strength of bucking.^{53–62} We will directly analyze *ab initio* data, as the sixteen band Liu-Allen model⁶³ does not faithfully capture topological properties.⁶⁴

Since Bi is a rhombohedral system with space group

$R\bar{3}m$ ⁶⁵, the BZ for primitive unit cell has the shape of truncated octahedron [see Fig. 6(a)]. The primitive reciprocal lattice vectors are given by Eq. 48, with $b = 0.384919$ and $g = 1.36307 \text{ \AA}^{-1}$.⁶⁶ All density-functional theory (DFT) are carried out with Quantum Espresso software package.^{67–69} Exchange-correlation potentials employ Perdew-Burke-Ernzerhof (PBE) parametrization

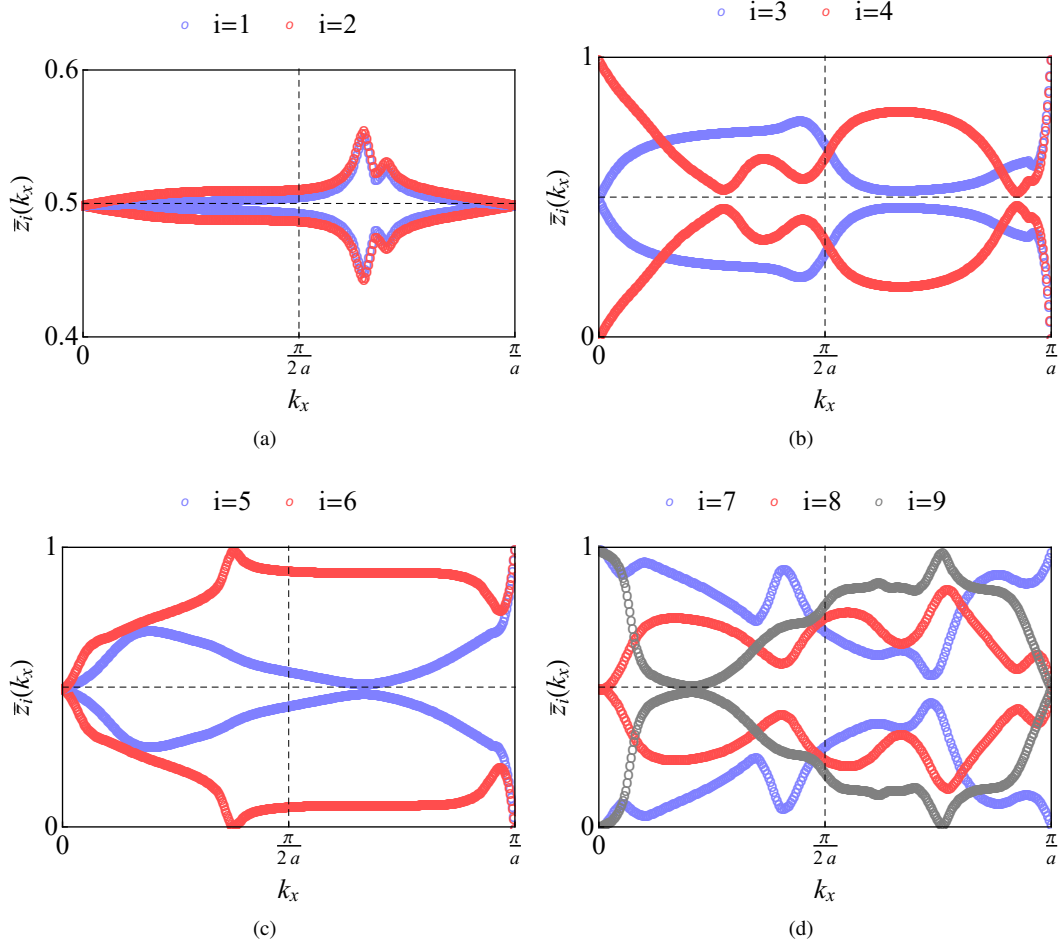


FIG. 10. Spectra of $SU(2)$ Wilson line $W_{z,i}(k_x, k_y = 0)$ for different bands. In precise agreement with results from previous section, (i) Class A bands (3, 5, 6, and 9) exhibit fully connected, gapless spectrum; (ii) Class B bands (4 and 7) possesses gapped spectrum; (iii) Class C bands (1, 2, and 8) display disconnected, gapless spectrum. The number of gapless points for bands 3, 5 and 6 [9] is one [3] and located at the $\bar{\Gamma}$ point [three \bar{M} points] of surface Brillouin zone. The total number of gapless points for class C bands is 4 ($\bar{\Gamma}$, and three \bar{M} points of surface Brillouin zone). As indicated by the staggered index, class B bands lack tunneling of Berry flux.

of generalized gradient approximation (GGA).⁷⁰ All topological analysis are performed with Wannier90 and Z2pack software packages.^{39,40,71}

The bulk band structure for primitive unit cell and coarse topological classification are respectively shown in Fig. 9(a) and Fig. 9(b). Bismuth is a compensated semimetal with band 5 (6) producing hole pocket around T point (electron pockets around L points). This does not affect topology of constituent bands. The hypothetical gapped, ground state, involving occupied bands 1 through 5 is a higher-order, TCI, with ground state indicators

$$\begin{aligned} & (\nu_{0,GS}; \kappa_{1,GS}; \kappa_{AF,GS}; \nu_{1,GS}; \nu_{2,GS}; \nu_{3,GS}) \\ & = (0; -2; +4; 0, 0, 0). \end{aligned} \quad (57)$$

Without considering rotation eigenvalues $e^{\pm i\pi}$ of band 5,

we would have found $\kappa_{AF,GS} = +2$.

To guarantee the absence of non-trivial Wilson lines through generic locations of hexagonal planes, we have computed WCCs ($\bar{z}_i(k_x, k_y)$) for different bands, which are displayed in Fig. 10. The results are in direct correspondence with those presented in Fig. 8(a)-8(c). Hence, we can conclude that class A, B, and C bands of Bi respectively support odd, zero, and even integer values of flux tunneling along C_3 axis. The calculation of mirror Chern numbers of occupied bands leads to

$$\mathfrak{C}_{m,YZ} = \text{diag}(0, 0, +1, 0, -1). \quad (58)$$

Again in full agreement with results of 4-band model, only class A bands are found to possess mirror Chern numbers. As bands 3 and 5 carry opposite mirror Chern numbers, the net mirror Chern number for the ground

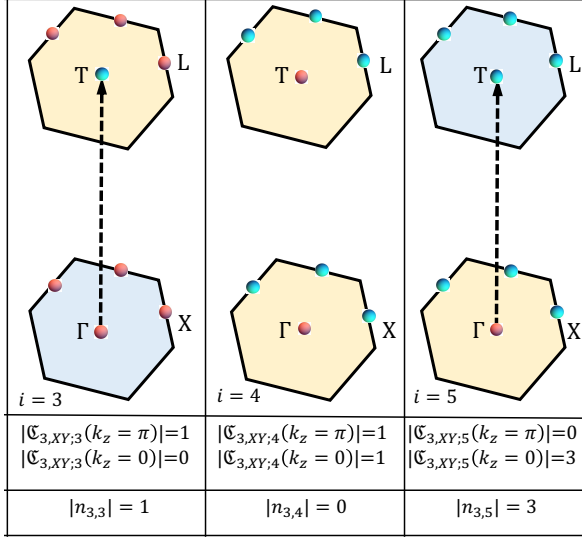


FIG. 11. Tunneling configurations of occupied bands $i = 3, 4, 5$, using conventional unit cell. The magnitudes of quantized Berry flux through 3-fold planes are found from in-plane Wilson loop calculations. The \mathbb{Z}_2 trivial (non-trivial) planes are colored light-blue (light yellow).

state vanishes.

The in-plane Wilson loop calculations for different bands also support classification based on κ_{AF} . Since the staggered index of bands 1 and 2 cancel each other, we only show the results for occupied bands 3, 4, and 5 in Fig. 11. Therefore, the ground state can carry net winding number ± 2 or ± 4 . This uncertainty can be resolved by implementing detailed gauge fixing process for Berry connection. As Bi is ultimately a semimetal, we do not pursue such numerically expensive analysis for *ab initio* band structure. However, in Appendix A, we address signed winding number of an 8-band tight-binding model of Bi⁴⁶, which can support ground state winding number 4.

VI. CONCLUSIONS

Our analysis for cubic model demonstrates the power of staggered index and Wilson loop for identifying signed 3D winding number for constituent Kramers degenerate bands and ground state. Similar analysis of tunneling of mirror Chern number can be carried out for tetragonal systems with space groups 83-88 (C_{4h} instantons) and 123-142 (D_{4h} instantons); hexagonal systems with space groups 174 (C_{3h} instantons), 175-176 (C_{6h} instantons), 187-190 (D_{3h} instantons), 191-194 (D_{6h} instantons). When high-symmetry planes lack mirror symmetry, the gauge-invariant magnitudes of relative Chern number and 3D winding number can be determined from Wilson loops, without detailed knowledge of underlying

ing basis. Therefore, a combined analysis of staggered index, in-plane Wilson loop, and straight Wilson lines are sufficient to perform \mathbb{N} classification of 3D winding numbers for all \mathcal{P} and \mathcal{T} symmetric systems. While the application of staggered index requires \mathcal{P} symmetry, Wilson loop calculations can be applied for addressing topology of \mathcal{PT} -preserving, magneto-electric systems.

Our work shows that states with $\kappa_{AF,GS} \neq 0$ can support $\sum_{j=1}^m n_{3,j} \neq 0$. Thus, we expect \mathbb{Z}_2 -trivial, topological crystalline insulators with $\kappa_{AF,GS} \neq 0$ to possess quantized, magneto-electric coefficient $\theta = 2s\pi$, with $s \in \mathbb{Z}$. The tight-binding model as well as *ab initio* band structure of bismuth support such conclusions. Can quantized topological response of such states be detected? To affirmatively answer this question, in Part II, we will probe topological response with magnetic monopole and vortices.

Appendix A: 8-band model of bismuth

The model is written using conventional unit cell, with BZ shown in. The Bloch Hamiltonian has the form

$$H(\mathbf{k}) = \begin{bmatrix} H_{TB,I}(\mathbf{k}) + \epsilon & \delta M_{TB}(\mathbf{k}) \\ \delta M_{TB}(\mathbf{k})^\dagger & H_{TB,II}(\mathbf{k}) - \epsilon \end{bmatrix}, \quad (\text{A1})$$

where $H_{TB,I/II}(\mathbf{k})$ describe two 4-band, strong \mathbb{Z}_2 topological insulators, coupled by the hybridization matrix $M_{TB}(\mathbf{k})$. The \mathcal{P} and C_{3z} for $H(\mathbf{k})$ follow as $\mathcal{P} = \mathcal{P}_I \oplus \mathcal{P}_{II}$ and $C_{3z} = C_{3z,I} \oplus C_{3z,II}$. For details of model parameters and explicit representations of symmetry operators, please consult the supplementary information of Ref. 46. Along the 3-fold axis all elements of M_{TB} vanish as a consequence of C_{3z} symmetry. The band structure and SIs are respectively shown in Fig. 12(a).

We will perform direct analysis of tunneling configurations of $SU(2) \times SU(2)$ Berry connection for occupied valence bands. From numerical results shown in Fig. 12(b), we find

$$(|\mathfrak{C}_{3,XY;1}|, |\mathfrak{C}_{3,XY;2}|)(k_z = 0) = (0, 0), \quad (\text{A2})$$

$$(|\mathfrak{C}_{3,XY;1}|, |\mathfrak{C}_{3,XY;2}|)(k_z = \pi) = (3, 1). \quad (\text{A3})$$

Thus, occupied bands 1 and 2 possess tunneling of Berry flux and the magnitudes of 3D winding numbers are

$$(|n_{3,1}|, |n_{3,2}|) = (3, 1). \quad (\text{A4})$$

Hence, the ground state can exhibit net even integer winding number $\pm 4, \pm 2$.

To resolve uncertainties, we have performed explicit Abelian gauge-fixing in the following manner. We first regulate the Bloch Hamiltonian as

$$H(\mathbf{k}) \rightarrow H(\mathbf{k}) + \alpha \Gamma_{NA} \quad (\text{A5})$$

where the traceless diagonal matrix

$$\Gamma_{NA} = \sigma_3 \otimes \sigma_3 \otimes \sigma_3, \quad (\text{A6})$$

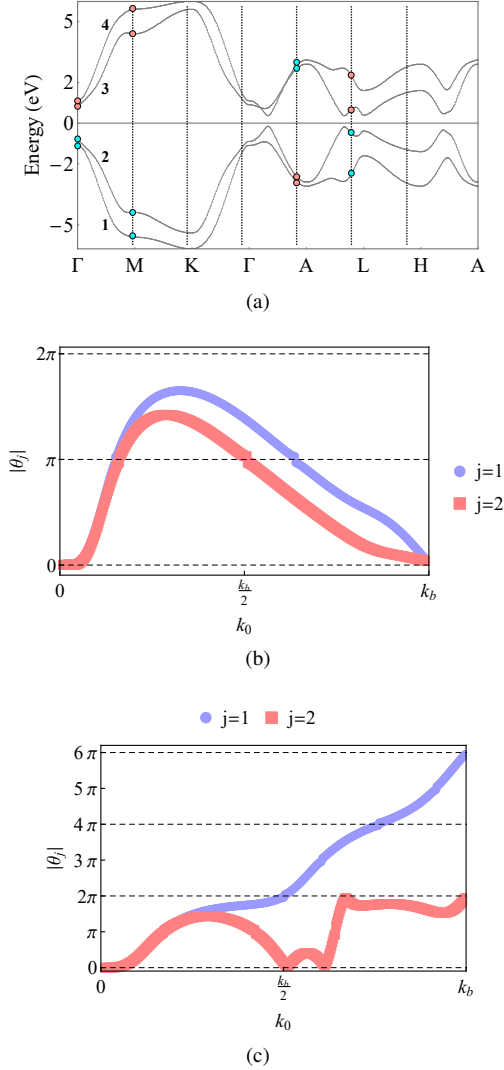


FIG. 12. (a) Band structure of 8-band tight-binding model, using hexagonal Brillouin zone for conventional unit cell. Parity eigenvalues +1 (-1) are labeled with red (cyan) dots. Bands are labeled by their energy at the Γ point, i.e. $E_1(0) < E_2(0) < E_3(0) < E_4(0)$. Results for $|\theta_j|$ (b) $k_z = 0$ and (c) $k_z = \pi$ planes, respectively.

is a generator of Cartan sub-algebra for the coset space, which commutes with $C_{3,z}$. This separates Kramers-pairs by $|2\alpha|$ at the BZ center. Appealing to Abelian Stokes theorem, the signed Berry flux for non-degenerate bands can be calculated with Abelian in-plane Wilson loops or TKNNY formula for Chern number⁷²

$$\mathfrak{C}_{3,XY;j} = \lim_{\alpha \rightarrow 0} \frac{1}{2\pi} \int_{T^2} d^2k F_j(\mathbf{k}) \quad (\text{A7})$$

where

$$F_j(\mathbf{k}) = \sum_{j \neq l} 2\text{Im} \frac{\langle \psi_{l,\mathbf{k}} | \partial_x \hat{H} | \psi_{j,\mathbf{k}} \rangle \langle \psi_{j,\mathbf{k}} | \partial_y \hat{H} | \psi_{l,\mathbf{k}} \rangle}{(E_{j,\mathbf{k}} - E_{l,\mathbf{k}})^2}.$$

By implementing this calculation, we find signed winding numbers

$$(\mathfrak{C}_{3,XY;1}, \mathfrak{C}_{3,XY;2})(k_z = 0) = (0, 0), \quad (\text{A8})$$

$$(\mathfrak{C}_{3,XY;1}, \mathfrak{C}_{3,XY;2})(k_z = \pi) = (+3, +1), \quad (\text{A9})$$

$$(n_{3,1}, n_{3,2}) = (+3, +1). \quad (\text{A10})$$

Therefore, the ground state of the 8-band model carries net 3D winding number +4.

If the hybridization matrix is switched off, the signed Berry flux and \mathcal{N}_3 for 4-band models $H_{TB,I}(\mathbf{k})$ and $H_{TB,II}(\mathbf{k})$ can be calculated following Secs. III and IV. The decoupled model also leads to Eq. A10 for constituent occupied bands. This demonstrates the stability of third homotopy classification determined from the tunneling configurations of non-Abelian Berry flux.

ACKNOWLEDGMENTS

This work was supported by the National Science Foundation MRSEC program (DMR-1720139) at the Materials Research Center of Northwestern University, and the start up funds of P. G. provided by the Northwestern University. A part of this work was performed at the Aspen Center for Physics, which is supported by National Science Foundation grant PHY-1607611.

¹ C. L. Kane and E. J. Mele, “ \mathbb{Z}_2 topological order and the quantum spin Hall effect,” *Phys. Rev. Lett.* **95**, 146802 (2005).
² B. A. Bernevig, T. L. Hughes, and S.-C. Zhang, “Quantum spin Hall effect and topological phase transition in HgTe quantum wells,” *Science* **314**, 1757–1761 (2006).
³ L. Fu, C. L. Kane, and E. J. Mele, “Topological insulators in three dimensions,” *Phys. Rev. Lett.* **98**, 106803 (2007).
⁴ Liang Fu and C. L. Kane, “Topological insulators with inversion symmetry,” *Phys. Rev. B* **76**, 045302 (2007).
⁵ J. E. Moore and L. Balents, “Topological invariants of time-

reversal-invariant band structures,” *Phys. Rev. B* **75**, 121306 (2007).

⁶ X.-L. Qi, T. L. Hughes, and S.-C. Zhang, “Topological field theory of time-reversal invariant insulators,” *Phys. Rev. B* **78**, 195424 (2008).

⁷ A. P. Schnyder, S. Ryu, A. Furusaki, and A. W. W. Ludwig, “Classification of topological insulators and superconductors in three spatial dimensions,” *Phys. Rev. B* **78**, 195125 (2008).

⁸ R. Roy, “ \mathbb{Z}_2 classification of quantum spin Hall systems: An approach using time-reversal invariance,” *Phys. Rev. B* **79**,

- 195321 (2009).
- ⁹ R. Roy, “Topological phases and the quantum spin Hall effect in three dimensions,” *Phys. Rev. B* **79**, 195322 (2009).
 - ¹⁰ S. Ryu, A. P. Schnyder, A. Furusaki, and A. W. W. Ludwig, “Topological insulators and superconductors: tenfold way and dimensional hierarchy,” *New J. Phys.* **12**, 065010 (2010).
 - ¹¹ M. Z. Hasan and C. L. Kane, “Colloquium: Topological insulators,” *Rev. Mod. Phys.* **82**, 3045–3067 (2010).
 - ¹² X.-L. Qi and S.-C. Zhang, “Topological insulators and superconductors,” *Rev. Mod. Phys.* **83**, 1057–1110 (2011).
 - ¹³ R.-J. Slager, A. Mesaros, V. Juričić, and J. Zaanen, “The space group classification of topological band-insulators,” *Nat. Phys.* **9**, 98–102 (2013).
 - ¹⁴ C.-K. Chiu, J. C. Y. Teo, A. P. Schnyder, and S. Ryu, “Classification of topological quantum matter with symmetries,” *Rev. Mod. Phys.* **88**, 035005 (2016).
 - ¹⁵ A. M. Essin, J. E. Moore, and D. Vanderbilt, “Magnetoelectric polarizability and axion electrodynamics in crystalline insulators,” *Phys. Rev. Lett.* **102**, 146805 (2009).
 - ¹⁶ A. M. Essin, A. M. Turner, J. E. Moore, and D. Vanderbilt, “Orbital magnetoelectric coupling in band insulators,” *Phys. Rev. B* **81**, 205104 (2010).
 - ¹⁷ A. Malashevich, I. Souza, S. Coh, and D. Vanderbilt, “Theory of orbital magnetoelectric response,” *New J. Phys.* **12**, 053032 (2010).
 - ¹⁸ S. Coh, D. Vanderbilt, A. Malashevich, and I. Souza, “Chern-simons orbital magnetoelectric coupling in generic insulators,” *Phys. Rev. B* **83**, 085108 (2011).
 - ¹⁹ N. Varnava, I. Souza, and D. Vanderbilt, “Axion coupling in the hybrid wannier representation,” *Phys. Rev. B* **101**, 155130 (2020).
 - ²⁰ J. Kruthoff, J. de Boer, J. van Wezel, C. L. Kane, and R.-J. Slager, “Topological classification of crystalline insulators through band structure combinatorics,” *Phys. Rev. X* **7**, 041069 (2017).
 - ²¹ B. Bradlyn *et al.*, “Topological quantum chemistry,” *Nature* **547**, 298–305 (2017).
 - ²² H. C. Po, A. Vishwanath, and H. Watanabe, “Symmetry-based indicators of band topology in the 230 space groups,” *Nat. Comms.* **8**, 1–9 (2017).
 - ²³ E. Khalaf, H. C. Po, A. Vishwanath, and H. Watanabe, “Symmetry indicators and anomalous surface states of topological crystalline insulators,” *Phys. Rev. X* **8**, 031070 (2018).
 - ²⁴ J. Cano, B. Bradlyn, Z. Wang, L. Elcoro, M. G. Vergniory, C. Felser, M. I. Aroyo, and B. A. Bernevig, “Building blocks of topological quantum chemistry: Elementary band representations,” *Phys. Rev. B* **97**, 035139 (2018).
 - ²⁵ M. G. Vergniory *et al.*, “A complete catalogue of high-quality topological materials,” *Nature* **566**, 480–485 (2019).
 - ²⁶ T. Zhang *et al.*, “Catalogue of topological electronic materials,” *Nature* **566**, 475–479 (2019).
 - ²⁷ F. Tang, H. C. Po, A. Vishwanath, and X. G. Wan, “Efficient topological materials discovery using symmetry indicators,” *Nat. Phys.* **15**, 470–476 (2019).
 - ²⁸ F. Tang, H. C. Po, A. Vishwanath, and X. G. Wan, “Comprehensive search for topological materials using symmetry indicators,” *Nature* **566**, 486–489 (2019).
 - ²⁹ M. G. Vergniory, B. J. Wieder, L. Elcoro, S. S. P. Parkin, C. Felser, B. A. Bernevig, and N. Regnault, “All topological bands of all stoichiometric materials,” arXiv:2105.09954 (2021).
 - ³⁰ Y. F. Xu, L. Elcoro, Z.-D. Song, B. J. Wieder, M. G. Vergniory, N. Regnault, Y. Chen, C. Felser, and B. A. Bernevig, “High-throughput calculations of magnetic topological materials,” *Nature* **586**, 702–707 (2020).
 - ³¹ L. Elcoro, B. J. Wieder, Z. D. Song, Y. F. Xu, B. Bradlyn, and B. A. Bernevig, “Magnetic topological quantum chemistry,” arXiv:2010.00598 (2020).
 - ³² A. Bouhon, G. F. Lange, and R.-J. Slager, “Topological correspondence between magnetic space group representations and subdimensions,” *Phys. Rev. B* **103**, 245127 (2021).
 - ³³ Gunnar F. Lange, Adrien Bouhon, and Robert-Jan Slager, “Subdimensional topologies, indicators, and higher order boundary effects,” *Phys. Rev. B* **103**, 195145 (2021).
 - ³⁴ D. S. Freed and G. W. Moore, “Twisted equivariant matter,” in *Ann. Henri Poincaré*, Vol. 14 (Springer, 2013) pp. 1927–2023.
 - ³⁵ N. Okuma, M. Sato, and K. Shiozaki, “Topological classification under nonmagnetic and magnetic point group symmetry: application of real-space Atiyah-Hirzebruch spectral sequence to higher-order topology,” *Phys. Rev. B* **99**, 085127 (2019).
 - ³⁶ R. Yu, X.-L. Qi, B. A. Bernevig, Z. Fang, and X. Dai, “Equivalent expression of \mathbb{Z}_2 topological invariant for band insulators using the non-abelian Berry connection,” *Phys. Rev. B* **84**, 075119 (2011).
 - ³⁷ A. Alexandradinata, X. Dai, and B. A. Bernevig, “Wilson-loop characterization of inversion-symmetric topological insulators,” *Phys. Rev. B* **89**, 155114 (2014).
 - ³⁸ M. Taherinejad, K. F. Garrity, and D. Vanderbilt, “Wannier center sheets in topological insulators,” *Phys. Rev. B* **89**, 1–14 (2014), 1312.6940.
 - ³⁹ D. Gresch, G. Autès, O. V. Yazyev, M. Troyer, D. Vanderbilt, B. A. Bernevig, and A. A. Soluyanov, “Z2pack: Numerical implementation of hybrid wannier centers for identifying topological materials,” *Phys. Rev. B* **95**, 075146 (2017).
 - ⁴⁰ A. A. Soluyanov and D. Vanderbilt, “Computing topological invariants without inversion symmetry,” *Phys. Rev. B* **83**, 235401 (2011).
 - ⁴¹ A. Bouhon, A. M. Black-Schaffer, and R.-J. Slager, “Wilson loop approach to fragile topology of split elementary band representations and topological crystalline insulators with time-reversal symmetry,” *Phys. Rev. B* **100**, 195135 (2019).
 - ⁴² B. Bradlyn, Z. Wang, J. Cano, and B. A. Bernevig, “Disconnected elementary band representations, fragile topology, and wilson loops as topological indices: An example on the triangular lattice,” *Phys. Rev. B* **99**, 045140 (2019).
 - ⁴³ S. Mao, A. Yamakage, and Y. Kuramoto, “Tight-binding model for topological insulators: Analysis of helical surface modes over the whole brillouin zone,” *Phys. Rev. B* **84**, 115413 (2011).
 - ⁴⁴ A. C. Tyner, S. Sur, D. Puggioni, J. M. Rondinelli, and P. Goswami, “Topology of three-dimensional Dirac semimetals and generalized quantum spin Hall systems without gapless edge modes,” arXiv:2012.12906v2 (2020).
 - ⁴⁵ A. C. Tyner *et al.*, “Quantized non-abelian, Berry’s flux and higher-order topology of Na_3Bi ,” arXiv:2102.06207 (2021).
 - ⁴⁶ F. Schindler *et al.*, “Higher-order topology in bismuth,” *Nat. Phys.* **14**, 918–924 (2018).
 - ⁴⁷ A. N. Rudenko, M. I. Katsnelson, and R. Roldán, “Elec-

- tronic properties of single-layer antimony: Tight-binding model, spin-orbit coupling, and the strength of effective coulomb interactions,” *Phys. Rev. B* **95**, 081407 (2017).
- ⁴⁸ S. H. Kim *et al.*, “Topological phase transition and quantum spin hall edge states of antimony few layers,” *Sci. Rep.* **6**, 1–7 (2016).
- ⁴⁹ S.-Y. Zhu *et al.*, “Evidence of topological edge states in buckled antimonene monolayers,” *Nano Lett.* **19**, 6323–6329 (2019).
- ⁵⁰ M. Bieniek, T. Woźniak, and P. Potasz, “Stability of topological properties of bismuth (1 1 1) bilayer,” *J. Condens. Matter Phys.* **29**, 155501 (2017).
- ⁵¹ C.-H. Hsu *et al.*, “Topology on a new facet of bismuth,” *Proc. Natl. Acad. Sci.* **116**, 13255–13259 (2019).
- ⁵² P. Hofmann, “The surfaces of bismuth: Structural and electronic properties,” *Prog. Surf. Sci.* **81**, 191–245 (2006).
- ⁵³ M. Wada, S. Murakami, F. Freimuth, and G. Bihlmayer, “Localized edge states in two-dimensional topological insulators: Ultrathin bi films,” *Phys. Rev. B* **83**, 121310 (2011).
- ⁵⁴ B. Rasche *et al.*, “Stacked topological insulator built from bismuth-based graphene sheet analogues,” *Nat. Mater.* **12**, 422–425 (2013).
- ⁵⁵ I. K. Drozdov *et al.*, “One-dimensional topological edge states of bismuth bilayers,” *Nat. Phys.* **10**, 664–669 (2014).
- ⁵⁶ L. Chen, Z. F. Wang, and F. Liu, “Robustness of two-dimensional topological insulator states in bilayer bismuth against strain and electrical field,” *Phys. Rev. B* **87**, 235420 (2013).
- ⁵⁷ A. K. Nayak *et al.*, “Resolving the topological classification of bismuth with topological defects,” *Sci. Adv.* **5**, eaax6996 (2019).
- ⁵⁸ A. Takayama, T. Sato, S. Souma, T. Oguchi, and T. Takahashi, “One-dimensional edge states with giant spin splitting in a bismuth thin film,” *Phys. Rev. Lett.* **114**, 066402 (2015).
- ⁵⁹ T. Lei *et al.*, “Electronic structure evolution of single bilayer bi (1 1 1) film on 3d topological insulator bi₂se₃ x te₃-x surfaces,” *J. Condens. Matter Phys.* **28**, 255501 (2016).
- ⁶⁰ T.-R. Chang *et al.*, “Band topology of bismuth quantum films,” *Crystals* **9**, 510 (2019).
- ⁶¹ S. Ito *et al.*, “Proving nontrivial topology of pure bismuth by quantum confinement,” *Phys. Rev. Lett.* **117**, 236402 (2016).
- ⁶² K. Saito, H. Sawahata, T. Komine, and T. Aono, “Tight-binding theory of surface spin states on bismuth thin films,” *Phys. Rev. B* **93**, 041301 (2016).
- ⁶³ Y. Liu and R. E. Allen, “Electronic structure of the semimetals Bi and Sb,” *Phys. Rev. B* **52**, 1566–1577 (1995).
- ⁶⁴ J. C. Y. Teo, L. Fu, and C. L. Kane, “Surface states and topological invariants in three-dimensional topological insulators: Application to Bi_{1-x}Sb_x,” *Phys. Rev. B* **78**, 045426 (2008).
- ⁶⁵ S. Golin, “Band structure of bismuth: Pseudopotential approach,” *Phys. Rev.* **166**, 643–651 (1968).
- ⁶⁶ A. Jain *et al.*, “Commentary: The materials project: A materials genome approach to accelerating materials innovation,” *APL Materials* **1**, 011002 (2013).
- ⁶⁷ P. Giannozzi *et al.*, “Quantum espresso: a modular and open-source software project for quantum simulations of materials,” *J. Phys. Condens. Matter* **21**, 395502 (19pp) (2009).
- ⁶⁸ P. Giannozzi *et al.*, “Advanced capabilities for materials modelling with quantum espresso,” *J. Phys. Condens. Matter* **29**, 465901 (2017).
- ⁶⁹ P. Giannozzi *et al.*, “Quantum espresso toward the exascale,” *J. Chem. Phys.* **152**, 154105 (2020).
- ⁷⁰ J. P. Perdew, K. Burke, and M. Ernzerhof, “Generalized gradient approximation made simple,” *Phys. Rev. Lett.* **77**, 3865 (1996).
- ⁷¹ P. Pizzi *et al.*, “Wannier90 as a community code: new features and applications,” *J. Phys. Condens. Matter* **32**, 165902 (2020).
- ⁷² D. J. Thouless, M. Kohmoto, M. P. Nightingale, and M. den Nijs, “Quantized Hall conductance in a two-dimensional periodic potential,” *Phys. Rev. Lett.* **49**, 405–408 (1982).